



Tumour-specific amplitude-modulated radiofrequency electromagnetic fields induce differentiation of hepatocellular carcinoma via targeting Ca_v3.2 T-type voltage-gated calcium channels and Ca²⁺ influx

Hugo Jimenez^a, Minghui Wang^a, Jacquelyn W. Zimmerman^{b,c}, Michael J. Pennison^a, Sambad Sharma^a, Trevor Surratt^a, Zhi-Xiang Xu^c, Ivan Brezovich^d, Devin Absher^e, Richard M. Myers^e, Barry DeYoung^f, David L. Caudell^f, Dongquan Chen^g, Hui-Wen Lo^a, Hui-Kuan Lin^a, Dwayne W. Godwin^h, Michael Olivierⁱ, Anand Ghanekar^j, Kui Chen^k, Lance D. Miller^a, Yijian Gong^l, Myles Capstick^l, Ralph B. D'Agostino Jr^m, Reginald Mundenⁿ, Philippe Merle^o, Alexandre Barbault^p, Arthur W. Blackstock^q, Herbert L. Bonkovsky^r, Guang-Yu Yang^s, Guangxu Jin^a, Liang Liu^a, Wei Zhang^a, Kounosuke Watabe^a, Carl F. Blackman^{a,*}, Boris C. Pasche^{a,*}

^a Department of Cancer Biology, Wake Forest Baptist Medical Centre, Winston-Salem, NC, United States of America

^b Department of Medicine, The Johns Hopkins School of Medicine, Baltimore, MD, United States of America

^c Division of Haematology/Oncology, The University of Alabama at Birmingham, Birmingham, AL, United States of America

^d Department of Radiation Oncology, The University of Alabama at Birmingham, Birmingham, AL, United States of America

^e HudsonAlpha Institute for Biotechnology, Huntsville, AL, United States of America

^f Department of Pathology, Wake Forest Baptist Medical Centre, Winston-Salem, NC, United States of America

^g Division of Preventive Medicine, The University of Alabama at Birmingham, Birmingham, AL, United States of America

^h Department of Neurobiology and Anatomy, Wake Forest Baptist Medical Centre, Winston-Salem, NC, United States of America

ⁱ Section of Molecular Medicine, Department of Medicine, Wake Forest Baptist Medical Centre, Winston-Salem, NC, United States of America

^j Department of Surgery, University Health Network, Toronto, Ontario, Canada

^k Toronto General Hospital Research Institute, Toronto, Ontario, Canada

^l IT'IS Foundation, Swiss Federal Institute of Technology, Zurich, Switzerland

^m Department of Biostatistical Sciences, Wake Forest Baptist Medical Centre, Winston-Salem, NC, United States of America

ⁿ Department of Radiology, Wake Forest Baptist Medical Centre, Winston-Salem, NC, United States of America

^o Croix-Rousse University Hospital, Hepato-Gastroenterology and Digestive Oncology, Lyon, France

^p TheraBionic GmbH, Ettlingen, Germany

^q Department of Radiation Oncology, Wake Forest Baptist Medical Centre, Winston-Salem, NC, United States of America

^r Section on Gastroenterology, Department of Medicine, Wake Forest Baptist Medical Centre, Winston-Salem, NC, United States of America

^s Department of Pathology, Northwestern University, Feinberg School of Medicine, Chicago, IL, United States of America

ARTICLE INFO

Article history:

Received 27 March 2019

Received in revised form 30 April 2019

Accepted 14 May 2019

Available online 31 May 2019

Keywords:

Advanced hepatocellular carcinoma
 T-type voltage gated calcium channels
 Calcium influx
 Ca_v3.2
 CACNA1H
 Amplitude-modulated
 Radiofrequency
 Electromagnetic fields
 AM RF EMF

ABSTRACT

Background: Administration of amplitude modulated 27·12 MHz radiofrequency electromagnetic fields (AM RF EMF) by means of a spoon-shaped applicator placed on the patient's tongue is a newly approved treatment for advanced hepatocellular carcinoma (HCC). The mechanism of action of tumour-specific AM RF EMF is largely unknown.

Methods: Whole body and organ-specific human dosimetry analyses were performed. Mice carrying human HCC xenografts were exposed to AM RF EMF using a small animal AM RF EMF exposure system replicating human dosimetry and exposure time. We performed histological analysis of tumours following exposure to AM RF EMF. Using an agnostic genomic approach, we characterized the mechanism of action of AM RF EMF.

Findings: Intrabuccal administration results in systemic delivery of athermal AM RF EMF from head to toe at levels lower than those generated by cell phones held close to the body. Tumour shrinkage results from differentiation of HCC cells into quiescent cells with spindle morphology. AM RF EMF targeted antiproliferative effects and cancer stem cell inhibiting effects are mediated by Ca²⁺ influx through Ca_v3.2 T-type voltage-gated calcium channels (CACNA1H) resulting in increased intracellular calcium concentration within HCC cells only.

Interpretation: Intrabuccally-administered AM RF EMF is a systemic therapy that selectively block the growth of HCC cells. AM RF EMF pronounced inhibitory effects on cancer stem cells may explain the exceptionally long

DOI of original article: <https://doi.org/10.1016/j.ebiom.2019.05.038>.

* Corresponding authors.

E-mail addresses: cblackma@wakehealth.edu (C.F. Blackman), bpasche@wakehealth.edu (B.C. Pasche).

<https://doi.org/10.1016/j.ebiom.2019.05.034>

2352-3964/© 2019 Published by Elsevier B.V. This is an open access article under the CC BY-NC-ND license (<http://creativecommons.org/licenses/by-nc-nd/4.0/>).

responses observed in several patients with advanced HCC.

Fund: Research reported in this publication was supported by the National Cancer Institute's Cancer Centre Support Grant award number P30CA012197 issued to the Wake Forest Baptist Comprehensive Cancer Centre (BP) and by funds from the Charles L. Spurr Professorship Fund (BP). DWG is supported by R01 AA016852 and P50 AA026117.

© 2019 Published by Elsevier B.V. This is an open access article under the CC BY-NC-ND license (<http://creativecommons.org/licenses/by-nc-nd/4.0/>).

1. Introduction

Hepatocellular carcinoma (HCC) death rates in the U.S. are increasing faster than for any other malignancy, having more than doubled in the past decade [1,2]. Worldwide, HCC is the fourth most common cause of cancer death and the second most common cause of absolute years of life lost due to cancer [3]. Despite the development and recent approval of additional treatment modalities [4–6], the outcome of patients with advanced HCC remains poor and new therapeutic approaches are sorely needed [4]. There is growing experimental and clinical evidence that alternating electric fields and amplitude-modulated electromagnetic fields are capable of blocking tumour growth [7]. However, little is known regarding the kHz to THz electromagnetic interactions with biological systems, which do not result in changes in temperature within tumour tissues or in tumour cell membrane electroporation.

We previously hypothesized [8] and subsequently provided experimental evidence that delivery of 27·12 MHz radiofrequency electromagnetic fields, which are amplitude-modulated at tumour-specific frequencies (AM RF EMF), has anticancer activity both *in vitro* [9] and in patients with advanced HCC and results in clinical benefits with min-

imal risks, even after several years of continuous daily use [10,11]. These clinical and translational findings led to the regulatory approval of the TheraBionic P1 AM RF EMF emitting device for the treatment of advanced hepatocellular carcinoma [12]. The medical device received European approval as a class IIa low-risk medical device in 2018 and is indicated for patients with advanced hepatocellular carcinoma who have failed or are intolerant to first line and second lines therapies.

Using HCC and breast cancer cell lines as well as immortalized hepatocytes and breast epithelial cells, we previously demonstrated that AM RF EMF control the growth of cancer cells at tumour-specific modulation frequencies but do not affect the growth of noncancerous cells [9]. While both alternating electric fields [13] and amplitude-modulated electromagnetic fields [9] have been shown to disrupt the mitotic spindle of tumour cells, the mechanism by which tumour-specific AM RF EMF result in tumour shrinkage and long-term therapeutic responses in patients with cancer is unknown [7]. Furthermore, the human dosimetry of intrabuccal administration has not been characterized.

Here we show that administration of amplitude-modulated radiofrequency electromagnetic fields by means of a spoon-shaped antenna placed on the patient's tongue results in systemic delivery of AM RF EMF with whole body averaged specific absorption rate (SAR) of 1·35 mW/kg with peak spatial SAR ranging from 146 to 352 mW/kg averaged over 1 g of tissue. Using a mouse exposure system replicating human exposure conditions [14], we show that AM RF EMF-mediated shrinkage of hepatocellular carcinoma results from differentiation of cancer cells into quiescent cells with spindle morphology. We identify Ca^{2+} influx through $\text{Ca}_v3\cdot2$ T-type voltage calcium channels (CACNA1H) resulting in increased intracellular calcium concentration as the necessary and sufficient initiating event of both AM RF EMF anti-proliferative effects on HCC cells and down-regulation of cancer stem cells, which likely accounts for the long-term responses observed in some patients with advanced HCC.

2. Materials and methods

2.1. Ethical statement

All procedures and protocols were performed in accordance with institutional guidelines and approved by the Wake Forest Institutional Animal Care and Use Committee (IACUC). The patient was offered compassionate treatment with the TheraBionic P1 device. Written informed consent that includes authorization to publish the patient's clinical data was obtained and compassionate use was approved by the Ethics Committee of the Cabinet Médical de l'Avenue de la Gare 6, 1003 Lausanne, Switzerland. Additionally, a compassionate use request for use a non-conforming medical device was submitted to and approved by Swissmedic: <https://www.swissmedic.ch/swissmedic/en/home/medical-devices/market-access/exemptions-for-non-conforming-medical-devices.html> Exemptions for non-conforming medical devices.

2.2. Dosimetry simulation

The primary purpose of the dosimetry assessment is to determine the safety of the device and provide insight into organ-specific absorption of AM RF EMF. The predicted absorption of intrabuccally-

Research in context

Evidence before study

We previously demonstrated that 27·12 MHz tumour-specific amplitude-modulated radiofrequency electromagnetic fields (AM RF EMF) administered intrabuccally result in tumour shrinkage or tumour control in 50% of patients with advanced hepatocellular carcinoma. We also showed that the same AM RF EMF block the growth of cancer cells *in vitro* but do not affect the growth of non-cancerous and non-corresponding tumour cells. While AM RF EMF have been shown to disrupt the mitotic spindle of tumour cells, the mechanism by which tumour-specific AM RF EMF result in tumour shrinkage and long-term therapeutic responses in patients with cancer is unknown. Additionally, the human dosimetry of AM RF EMF intrabuccal administration has not been characterized.

Added value of this study

This study shows that intrabuccally-delivered AM RF EMF result in whole-body absorption below international standards for safety exposure. Hepatocellular carcinoma shrinkage upon treatment with tumour-specific AM RF EMF results from differentiation of tumour cells into quiescent cells with spindle morphology. Targeted inhibition of hepatocellular carcinoma cell growth and downregulation of cancer stem cells is initiated by calcium influx through $\text{Ca}_v3\cdot2$ T-type voltage-gated calcium channels (CACNA1H).

Implication of all the available evidence

These findings unveil the mechanism of action of tumour-specific AM RF EMF.

administered 27·12 MHz AM RF EMF and the observed clinical results showing shrinkage of the primary and/or metastatic tumours in several parts of the body of several patients prompted us to systematically characterize the overall and organ-specific levels of AM RF EMF delivered during treatment with the TheraBionic device [8,10]. As previously described, the AM RF EMF generator is a battery-driven device connected to a 1·5 m long 50 Ω coaxial cable, which ends with a stainless-steel spoon-shaped mouthpiece connected via an impedance transformer [8,10]. The device operates at a carrier frequency of 27·12 MHz. The carrier frequency is amplitude-modulated at tumour-specific frequencies with 85% modulation depth, sequentially switched every three seconds from the lowest to the highest frequency in the range of 0·01 Hz to 150 kHz. Dosimetry simulation, performed with SEMCAD X, was based on the adult male anatomical model Duke (weight 73 kg) of the 'Virtual Population' [15]. For simplicity, the TheraBionic device is represented by a metal box of dimensions 80 mm \times 60 mm \times 160 mm, covered with a plastic layer. The wire, modelled as one metre in length, is connected to a metal block of size 5 mm \times 30 mm \times 50 mm to mimic the spoon-shaped mouthpiece, which is placed on the anterior part of the human model's tongue. The simulation is set with two millimetres resolution for humans at a frequency of 27·12 MHz. The total power delivered, SAR distribution, and the organ specific SAR are assessed, and compared with the experimental results based on a similar but simplified scenario. The scenarios of the different treatments are selected based on the three most common postures used with the device, which are shown in Fig. 1c: 1) sitting with the device on the leg; 2) sitting with the device on the abdomen; 3) sitting with the device placed away from the body. 4) is a theoretical position to test the hypothesis that the body can act as one half of a short dipole antenna – with the cable and device forming the other half – that occurs when the device is placed away from the head and aligned with the body and the patient lying down. These human postures are first simulated on homogeneous models with dielectric parameters of muscle ($\epsilon_r = 95\cdot9$ and $\sigma = 0\cdot65$ S/m), which provides a general view of the power dissipation and SAR distribution in the human models. Furthermore, inhomogeneous human models – with all tissues segmented and allocated appropriate electrical properties – are simulated for two of the four cases, 1) and 3), which are the two most common postures adopted by patients receiving treatment, to verify the power dissipation and SAR distribution compared with the homogeneous model and to analyse the organ-specific SAR.

2.3. Dosimetry experimental validation

The validation measurements are based on a tank phantom due to its simple construction and higher SAR levels for given input power. The size of the chosen tank is 100 mm \times 150 mm \times 890 mm, with a tissue simulating liquid composed of saline with $\epsilon_r = 78\cdot9$ and $\sigma = 0\cdot435$ S/m. Similar configurations in geometry are used as for human body simulation, thus allowing the same degree of comparison, and are shown in Fig. 1f. In each configuration, two lines in the tank have been measured with SPEAG's Dosimetric Assessment System (DASY) with EX3DV3 probe S/N 3515 (SPEAG, Switzerland); one line is 5 mm above the spoon position, and the other is 5 mm above the bottom of tank. These measured results are compared to the corresponding tank simulation to verify the simulation reliability.

2.4. AM RF EMF exposure in vitro

Cell lines were exposed to 27·12 MHz radiofrequency electromagnetic fields using exposure systems designed to replicate clinical exposure levels. Experiments were conducted at SARs of 30 and 400 mW/kg. Cells were exposed for 3 h daily, seven days in a row. Cells were exposed to tumour-specific modulation frequencies that were previously identified by changes in pulse pressure [8] in patients with a diagnosis of HCC [10] or modulation frequencies never identified in patients with a diagnosis of cancer. Specifically, the randomly chosen

frequencies have been selected at random in the range of 500 Hz to 22 kHz, i.e., within the same range as the hepatocellular carcinoma-specific and breast cancer-specific frequencies. The only selection criterion within this range was for frequencies to be at least 5 Hz higher or lower than any hepatocellular carcinoma-specific or breast cancer-specific frequency identified in patients with the corresponding diagnoses [8–10]. We have previously reported that the primary method for identification of tumour-specific frequencies is an increase in the amplitude of the pulse for one or more beats during scanning of frequencies [8]. Using the same method, we monitored variations in the amplitude of the radial pulse in thirty patients with a diagnosis of cancer and did not observe any change in pulse amplitude during exposure to the randomly chosen frequencies [8].

2.5. Cell lines

HCC cell lines of various ethnic background, HepG2 (Caucasian), Hep3B (African American, hepatitis B positive) and Huh7 (Asian), HCCLM3 (Asian, hepatitis B positive), and MHCC97-L (Asian, hepatitis B positive) were used as models of representation for HCC. THLE2 is an immortalized non-malignant hepatocyte cell line. HepG2, Hep3B, THLE2, H9c2(2–1) (Rat Myocardium), and HMC3 (Human microglia) cells were purchased from ATCC (Manassas, VA) and Huh7 cells were purchased from Creative Bioarray (Shirley, NY). HCCLM3 and MHCC97-L were a gift from the Liver Cancer Institute, Fudan University, China. The Huh7/GFP cells were established by infection with lentiviruses expressing Lv-EF1 α -puro-GFP (SignaGen, Rockville, MD) followed by selection with 1 μ g/mL puromycin for two weeks. Pools of puromycin-resistant stable clones were collected. Expression of GFP was determined by western blot and fluorescent microscopy.

2.6. [³H] thymidine incorporation assay

Growth inhibition (GI) was assessed in HCC cells exposed to HCC-specific modulation frequencies as previously described. Briefly, following six days of AM RF EMF exposure, on the seventh and final day of exposure 3uCi ³H Thymidine (Perkin-Elmer) is added to each well (i.e. ³H concentration = 1uCi of ³H per mL of media) and then the final exposure session (3 h long @ 37 °C) will take place with one additional hour of incubation at 37 °C. Following the 4 h of total incubation time, the ³H containing media is removed and the 35 mm dishes or six-well plates are washed with 1x with cold PBS for 5 min with constant gentle rocking/agitation. After 5 min, PBS is removed and 800uL of 0·2 N NaOH is added to each well/dish. Place on rocker for a minimum of 1 h, up to overnight, of gentle agitation to lyse cells. Afterwards, transfer lysate to a seven millilitres scintillation vial containing four millilitres of Ultima Gold (Perkin Elmer) scintillation fluid and read with a scintillation counter (Beckman Coulter).

2.7. Gene expression analysis

RNA extraction from cells was performed by using RNeasy Mini Kit or miRNeasy Mini Kit (QIAGEN). qRT-PCR was performed using a Roche LightCycler II and 1-Step Brilliant II SYBR Green qRT-PCR master mix kit (Agilent Technologies). Data for qRT-PCR were expressed as mean \pm SEM and statistical differences between groups were calculated by a two-tailed Student *t*-test.

2.8. shRNA knockdown of T-type voltage-gated calcium channels

The specific knockdown of all three T-type VGCC isoforms Huh7 and Hep3B cells were accomplished by using the following kits. CACNA1g Human shRNA Plasmid Kit [Locus ID 8913] (Cat# TL305680 ORIGENE); CACNA1h Human shRNA Plasmid KIT [Locus ID 8912] (Cat# TL314243 ORIGENE); CACNA1i Human shRNA Plasmid Kit [Locus ID 8911] (Cat# TL314242 ORIGENE).

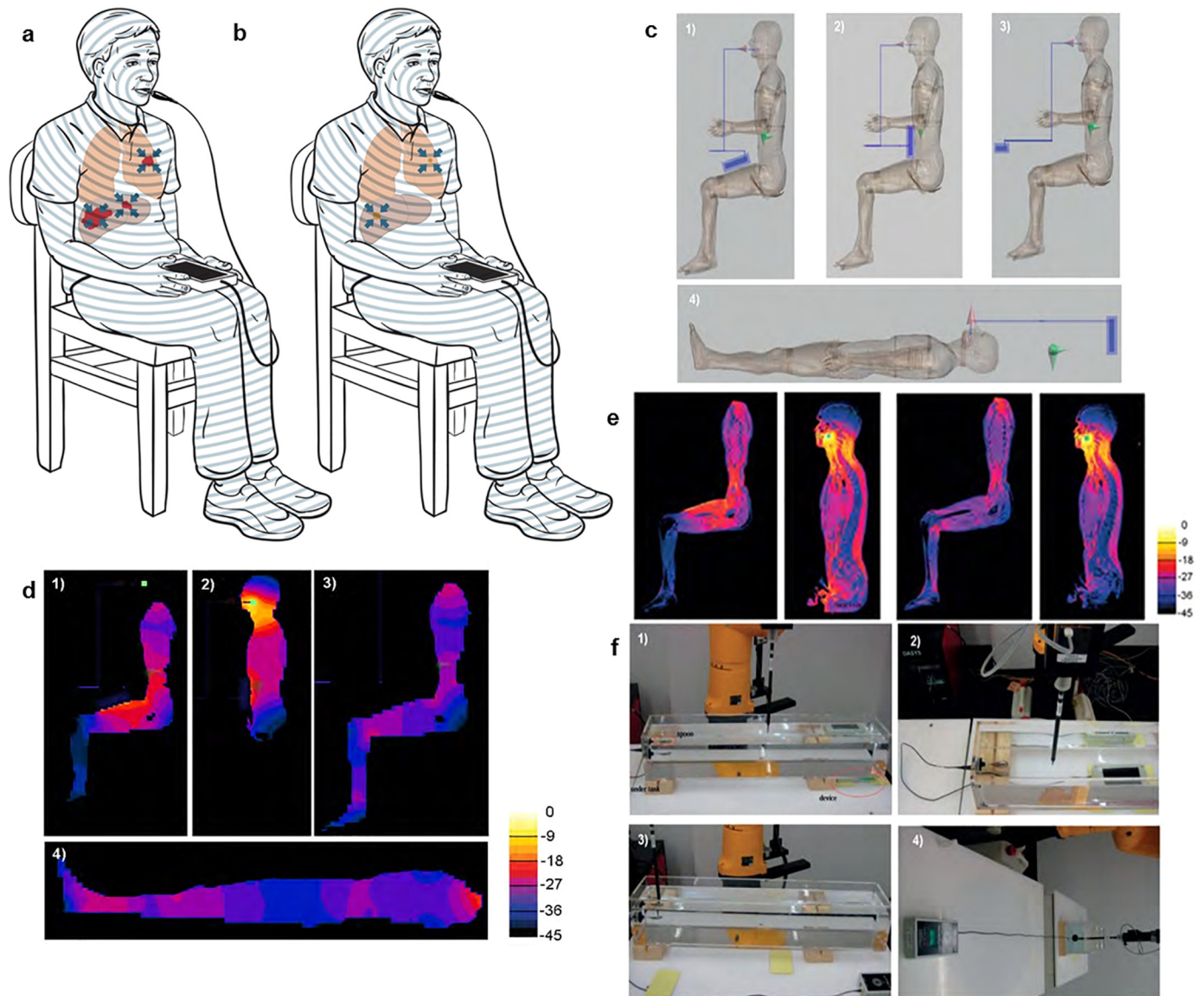


Fig. 1. Intrabuccal delivery results in systemic absorption of AM RF EMF. a Patient with advanced hepatocellular carcinoma receiving first treatment with the AM RF EMF emitting device. The concentric lines represent AM RF EMF emission from the spoon-shaped antenna placed on the patient's tongue. Red: primary and metastatic tumours. Blue arrows: depiction of antitumor activity location. b Same patient several months later with evidence of shrinkage or disappearance of the primary tumour and its metastases [10,11]. Brown: shrunk tumour following AM RF EMF treatment, c,1) Patient sitting with device on thigh, 2) Patient sitting with device on the abdomen, 3) Patient sitting with device placed away from the body, 4) Patient in supine position to test the hypothesis that the body can act as one half of a short dipole antenna while the cable and device form the other half, or for treatment lying down while the device is behind the head. The device and coaxial cable are shown in blue. The electric dipole is shown in green. d, SAR slice views in the homogeneous human model: the images are normalized to 5 W/kg/W, with 3 dB/contour. 1) Patient sitting with device on thigh, 2) Patient sitting with device on the abdomen, 3) Patient sitting with device placed away from the body, 4) Patient in supine position. e, SAR slice views in the inhomogeneous model: the images are normalized to 5 W/kg/W, with 3 dB/contour. Left panels: patient sitting with device on thigh. Right panels: patient sitting with device located away from the body. f, Experimental validation measurements setups and results. 1) The device is located at one extremity underneath the tank, 2) The device is in the middle underneath the tank, 3) The device is beside the tank, 4) The device is as far away from the tank as possible.

2.9. Quantitative real-time PCR target primers and machine protocol

CACNA1g (CAV 3·1)-Forward primer: 5' CTT ACC AAC GCC CTA GAA ATC A 3'; CACNA1g (CAV 3·1)-Reverse primer: 5' GAT GTA GCC AAA GGG ACC ATA C 3'; CACNA1h (CAV 3·2)-Forward primer: 5' CAA GGA TGG ATG GGT GAA CA 3'; CACNA1h (CAV 3·2)-Reverse primer: 5' GAT GAG CAG GAA GGA GAT GAA G 3'; CACNA1i (CAV 3·3)-Forward primer: 5' GCC CTA CTA TGC CAC CTA TTG 3'; CACNA1i (CAV 3·3)-Reverse primer: 5' AGG CAG ATG ATG AAG GTG ATG 3'; GAPDH-Forward primer: 5' TGC ACC ACC AAC TGC TTA GC 3'; GAPDH-Reverse primer: 5' GGC ATG GAC TGT GGT CAT GAG 3'; MIR-1246-Forward primer: 5' CCG TGT ATC CTT GAA TGG ATT T 3'; MIR-1246-Reverse primer: 5' CAT TGC TAG CCT ATG GAT TGA TTT 3'; HSA-LET-7G-

Forward primer: 5' GCT GAG GTA GTA GTT TGT ACA GTT 3'; HSA-LET-7G-Reverse primer: 5' GCA GTG GCC TGT ACA GTT AT 3'; RPLPO-Forward primer: 5' TTC ATA CCC AGC TAG CCA ATC 3'; RPLPO-Reverse primer: 5' TTT CCA TCC CAC TCC CTT TC 3'; All primers were purchased from IDT. Roche LightCycler 489 Instrument II Protocol: 1 cycle for 30 min at 50 °C, 1 cycle for 10 min at 95 °C, 40 × (30 s at 95 °C / 1 min at 60 °C), Rest at 4 °C.

2.10. Fluo-4 Ca²⁺ imaging

Huh7 cells – seeded into six-well plates or 35 mm dishes (Falcon; Corning) – before receiving either AM RF EMF treatment. 300,000 cells were left to adhere overnight and cultured in Dulbecco's Modified

Eagle's Medium (DMEM; Cellgro) supplemented with heat-inactivated foetal bovine serum (FBS, final concentration 10%; Atlanta Biologicals). Cells were exposed to either HCCMF (hepatocellular carcinoma specific AM RF EMF) or no treatment for 30 min, 1 h, 3 h, or 6 h. 30 min before completion of treatment Fluo-4 stain mix was added directly to each well/dish (Fluo-4 Calcium Imaging Kit; Molecular Probes). Dishes/plate were placed on a rocker at room temperature for 5 min of gentle distribution of Fluo-4 stain. Cells were then placed back into the 37 °C incubator and exposed for 30 min to HCCMF (completing the required time of HCCMF exposure). Following completion of treatment exposure, the dishes/plates were placed at room temperature for 30 min (in the dark). Cells were then washed using 1.5 mL of LCIS (Live Cell Imaging Solution; Molecular Probes) then placed in two millilitres of fresh LCIS and fluorescent intensity was read using a Fluostar fluorescent plate reader (BMG LABTECH) (485 excitation/520 emission). All experiments were performed at least twice with representative experiments shown. Statistics: one-way *t*-test was utilized.

2.10.1. Fluo-4 Ca^{2+} imaging with VGCC blocker

T-type VGCC 2-ethyl-2-methylsuccinimide (ethosuximide, ETHOS group) (0.5 mM final concentration) (Sigma-Aldrich). Amlodipine besylate (1 μ M final concentration) (Sigma-Aldrich). Ethosuximide or amlodipine was dissolved in 100% ethanol as the vehicle control (VC) (Fisher) as per Sigma-Aldrich recommendation to create working solution. Ethosuximide, amlodipine or vehicle was added to each well 30 min before start of treatment. Following 30 min of incubation at 37 °C, the Fluo-4 experiment proceeded as stated in the above protocol (three-hour exposure).

2.11. Extracellular Ca^{2+} chelation

Huh7 cells – seeded in 35 mm dishes, six dishes per group – were cultured in the presence or absence of the extracellular Ca^{2+} chelator 1,2-bis(2-aminophenoxy) ethane-N,N',N'-tetraacetic acid (BAPTA; Sigma-Aldrich). BAPTA was dissolved in dimethyl sulfoxide (DMSO; Fisher), as per Sigma-Aldrich recommendations, to create a working solution. The AM RF EMF treatment groups were as follows: HCCMF, randomly chosen, HCCMF + BAPTA, randomly chosen + BAPTA. Cells were left to adhere overnight then were cultured in Dulbecco's Modified Eagle's Medium (DMEM; Cellgro) supplemented with heat inactivated foetal bovine serum (FBS, final concentration 10%; Atlanta Biologicals). Cells were exposed to either HCC-specific or randomly chosen frequencies daily for 3 h in a row, either in the presence or absence of BAPTA (final concentration 100 μ M). The BAPTA working solution was added to the culture medium within 5 min before exposure to HCC-specific or randomly chosen frequencies. Within 5 min after completion of the three-hour exposure time, the BAPTA-containing media was discarded and replaced with fresh media without BAPTA. On day seven, cell proliferation was assessed with the tritiated thymidine incorporation assay. Experiments were repeated twice. Statistics: We fit a two-way ANOVA model to examine the effect of experiment (first/s) and group (four-levels: HCCMF, randomly chosen, HCCMF + BAPTA, and randomly chosen + BAPTA).

2.12. L-type and T-type voltage gated calcium channel blockade

2.12.1. L-type VGCC blockade

Huh7 cells were seeded in 6-well plates and cultured in the presence or absence of a L-type voltage gated calcium channel (VGCC) blocker, nifedipine, (Sigma-Aldrich). Nifedipine was dissolved in dimethyl sulfoxide (DMSO; Fisher), as per Sigma-Aldrich recommendations, to create working solution. The treatment groups were as follows: HCCMF, randomly chosen frequencies, HCCMF + nifedipine, and randomly chosen frequencies + nifedipine. Cells were left to adhere overnight and then were cultured in Dulbecco's Modified Eagle's Medium (DMEM; Cellgro) supplemented with heat inactivated FBS (final concentration 10%). Cells

were exposed to either HCC or randomly chosen frequencies (RCF) daily for 3 h in a row, either in the presence or in the absence of nifedipine (final concentration 100 μ M or 10 μ M). Nifedipine working solution was added to the culture medium within 5 min before exposure to HCCMF or RCF. Within 5 min after completion of the three-hour exposure time, media was removed from all dishes and replaced with fresh media, not containing nifedipine. On day seven, cell proliferation was assessed with the tritiated thymidine incorporation assay. The experiment was repeated twice.

2.12.2. T-type VGCC blockade

Huh7 cells were seeded in six-well plates at 20,000 cells per dish and cultured in the presence or absence of a pan T-type VGCC 2-ethyl-2-methylsuccinimide (ethosuximide, ETHOS group) (1 mM) (Sigma-Aldrich). Ethosuximide was dissolved in 100% ethanol as the vehicle control (VC) (Fisher) as per Sigma-Aldrich recommendation to create working solution. The treatment groups were as follows: SHAM (VC), RCF (VC), HCCMF (VC), SHAM (ETHOS), RCF (ETHOS) and HCCMF (ETHOS). Cells were left to adhere overnight and were then cultured in Dulbecco's Modified Eagle's Medium (DMEM; Cellgro) supplemented with heat inactivated FBS (final concentration 10%). Cells were exposed to either HCCMF or RCF daily for 3 h in a row or received no treatment, either in the presence or in the absence of ethosuximide (final concentration 1 mM). Ethosuximide working solution was added to the culture medium within 10 min before exposure to HCCMF, RCF, or SHAM groups. Within 5 min after completion of the three-hour exposure time, media was removed from all dishes and replaced with fresh media without ethosuximide. On day seven, cell proliferation was assessed with the tritiated thymidine incorporation assay, flow cytometry markers were stained, or cells were cultured in tumour sphere media for sphere formation assays. Experiments were repeated at least twice. Statistics: One-way ANOVA was used to statistically compare the effect of experimental (HCCMF) and control groups (SHAM and randomly chosen frequencies). Post hoc testing was by the Tukey test. Data are expressed as mean \pm SEM. Graphpad Prism was the software used for statistical analysis.

2.13. Flow cytometry analysis

Cells cultured, divided and treated into HCCMF, RCF or SHAM groups. After seven days of treatment cells were labelled for CD44-APC (mouse anti-human 1:20,000(Huh7) and 1:10(Hep3B), Cat#103011 Biologend) and CD133-PE (mouse anti-human 1:10 (Huh7) and 1:20(Hep3B), Cat# 130-098-826 Miltenyi Biotec) markers of cancer stem cell, fixed and analysed via flow cytometry. Data collection was performed on a C6 Accuri flow cytometer while analysis was performed on CFlow Plus software (Becton Dickinson).

2.14. Sphere formation assay

Cells were cultured, divided and treated in HCCMF, RCF or SHAM groups. Cells were plated (200 cells/well) in 96-well ultra-low attachment plates (Corning) with DMEM/F12 supplemented with 2% B27 (Invitrogen), 20 ng/mL EGF (Sigma Aldrich), and 4 μ g/mL insulin (Sigma-Aldrich). Cells seeded at a density of 100–500 viable cells per 100 μ L. Five-seven days post-treatment cells were counted for the number of spheres present in each well and data were represented as the means \pm SEM.

2.15. In vivo effects of amplitude-modulated radiofrequency electromagnetic fields

To replicate the dosimetric conditions resulting from intrabuccal administration of AM RF EMF in vivo, we designed and developed a small animal exposure system for AM RF EMF [14]. This exposure system allows for control of SAR levels in the same range as those generated by

intrabuccal administration [14]. Mice were exposed to RF EMF amplitude-modulated at the previously published hepatocellular carcinoma specific (HCCMF) [9] or randomly chosen (RCF) [9] frequencies 3 h daily. Another group of control mice was not exposed to any RF EMF. A total of 40 non-obese diabetic severe combined immunodeficient (NOD SCID; Jackson labs) mice (male and female) were used. Mice were housed in plastic cages with up to five mice/cage at room temperature and fed a standard mouse diet with water ad libitum (food and water were autoclaved). Mice were injected subcutaneously in the right hind flank with 7.0×10^6 Huh7 cells, re-suspended in 200 μ L of DPBS, at five-seven weeks of age. Thirty-seven of the 40 (92.5%) mice developed palpable Huh7 tumours. Upon establishment of a palpable tumour, measuring at a minimum of 0.5 cm in one dimension (Length or Width), mice were randomly assigned and exposed to HCCMF or RCF 3 h daily. An additional group of mice were not exposed to any RF EMF (SHAM treatment group). Mice set to receive AM RF EMF exposure were placed in a custom-designed exposure system [14], consisting of two transverse electromagnetic (TEM) cells configured as half-wave resonators (sXv-27, IT'IS, Zurich, Switzerland). Mice were exposed to 27.12 MHz EMF, modulated at HCC [9] or randomly chosen [9] frequencies set to result in an organ-specific SAR of 67 mW/kg within subcutaneous tumours, i.e., tumours located in the subcutaneous fat [14]. Tumours were measured with callipers three times per week. Mice were euthanized when tumour burden was excessive; 2 h before euthanasia, a total of 12 mice (6 exposed to HCCMF, 3 exposed to RCF, 3 not exposed to EMF; SHAM) were injected intraperitoneally with 200 μ L bromodeoxyuridine labelling reagent (BrdU; Life Technologies). Mouse tissue and xenograft tumour were collected/fixed for paraffin embedding and evaluated by immunohistochemistry.

2.16. Mice carrying patient derived xenografts

10 NSG female mice, with PDX implanted tumours, were provided by Anand Ghanekar M.D. from University Health Network (UHN) (Toronto, Ontario, Canada). Briefly, the patient derived tumour was from a 63-year-old male HCC patient with negative viral serologies, no metastases to lymph nodes, positive for microscopic and large vessel vascular invasions, multiple satellites/intrahepatic metastatic smaller nodules, TNM stage: pT3bN0 and no significant fibrosis or other active parenchymal or biliary injury. The tumour was implanted into immunocompromised (NSG) mice as previously described [16]. After one month of quarantine, six mice were exposed to HCC-specific AM RF EMF, and four mice were observed as controls. In total, mice received HCCMF for eight weeks.

2.17. Statistics

In vivo tumour volume comparisons were accomplished by repeated measures mixed models analysis. In these models, group and time were fixed effects and the individual animals were treated as random effects. A time by group interaction was examined to determine if tumour growth rates were different between groups. If the time by group interaction was found to be significant, the mixed models were fit again stratified by time to allow for groups to be compared at individual time points to determine when the observed effects became statistically significant.

2.18. Immunohistochemistry

Xenografts were fixed in 10% neutral buffered formalin (NBF), sectioned at 4 μ m and stained for the following: Cyclin D1 [92G2] (Rabbit anti-human 1:100, #2978 s Cell Signalling Technology); Ki-67 [D2H10] (Rabbit anti-human 1:800, #9027 s Cell Signalling Technology); p21 Waf1/Cip1 [DCS60] (Mouse anti-human 1:100, #2946 s Cell Signalling Technology); S100B [9A11B9] (Mouse anti-human 1:100, sc-81,709 Santa Cruz Biotechnology); BrdU [Bu20a] (Mouse anti-

human 1:400, #5292 s Cell Signalling Technology); PCNA [PC10] (Mouse anti-human 1:8000, #2586 s Cell Signalling Technology); Green Fluorescent Protein (GFP) (Rabbit 1:400, #2555 s Cell Signalling Technology); SLUG [A-7] (Mouse anti-human (no results), sc-166,476 Santa Cruz Biotechnology); E-Cadherin [HECD-1] (Mouse anti-human 1:100, ab1416 ABCAM); N-Cadherin [D4R1H] XP (Rabbit anti-human 1:125, #13116 Cell Signalling Technology); SNAI1 [OT15E12] (Mouse anti-human 1:25), TA500316 ORIGENE); Alpha Smooth Muscle Actin (Rabbit anti-human 1:200, ab5694 ABCAM); Vimentin [V9] (Mouse anti-human 1:1200, ab8069 ABCAM); Fibronectin [F1] (Rabbit anti-human 1:300, ab32419 ABCAM); Twist [10E4E6] (Mouse anti-human 1:100, ab175430 ABCAM); The small bowels of mice were fixed in 10% neutral buffered formalin and stained for BrdU (1:400). Average number of positive staining cells was counted in a blinded fashion for both control and treated groups. Tumour samples were from mice with established tumour after subcutaneous xenograft injection of the Huh7 cells, having received HCC-specific, randomly chosen frequencies or SHAM treatment for ten weeks. EMT panel staining and GFP tagged IHC slides were prepared and digitally scanned by the Wake Forest Baptist Comprehensive Cancer Centre Tumour Tissue and Pathology Shared Resource. All images were prepared with Nano Zoomer Digital pathology software (Hamamatsu Photonics K.K.) from digital slide scans (1x and 20x magnification). IHC staining was performed by Dr. David Caudell. Visualization and quantification were performed blindly by Dr. Barry DeYoung, average number of positive staining cells was counted for both control and treated groups. Tumour samples were from mice with established tumour after subcutaneous xenograft injection of the Huh7 cells, having received HCCMF or SHAM treatment for ten weeks. Statistics: One-way Analysis of Variance (ANOVA) was used to statistically compare the effect of experimental (HCCMF) and control groups (SHAM & RCF). Post-Hoc testing was compared by a Tukey Test. Data for Immunohistochemistry were expressed as mean \pm SEM. Graphpad Prism was the software used for statistical analysis. IHC was performed on a Leica Bond RX (Leica Biosystems, Buffalo Grove, IL) automated stainer.

2.19. RNA-Seq data analysis

We have generated two RNA-Seq data sets using two cell lines, Huh7 and HepG2. The RNA-Seq data of Huh7 include six controls and six treated samples. The HepG2 dataset contains two controls and two treated samples. The alignment and quality control of RNA-Seq data followed the pipeline developed by the NCI's Genomic Data Commons (GDC, <https://gdc.cancer.gov/>). The alignment was performed using a two-pass method with STAR2 [17]. The quality assessment was carried out by FASTQC (<https://www.bioinformatics.babraham.ac.uk/projects/fastqc/>) on the pre-alignment, and RNA-SeQC [18] and Picard tools (<http://broadinstitute.github.io/picard/>) on the post-alignment. Read Counts were performed by Summarized Experiment of DESeq2 [19]. The count data were normalized by betweenLaneNormalization function of EDASeq [20] to normalize the data using upper-quartile (UQ) normalization and then estimate the factors of unwanted variation using empirical control genes, e.g., least significantly differentially expressed (DEGs) genes based on a first-pass DEG analysis performed prior to RUVg normalization [21]. Lastly, DEG analysis is implemented by DESeq2 by adding the factors of unwanted variation into design of DESeq2 in order to remove unwanted variation. MicroRNA arrays: the initial microRNA array analysis did not reach any significance. Eighty percent of miRs are not expressed and should not be penalized. After adjustment for the lack of expression of 80% of the miRs, miR-1246 was the most significant miR showing differential expression in both HepG2 and Huh7. There are additional miRs that are invariably significant in addition to miR-1246: miR-4306, 378b, 1973, 3175, which are similarly more expressed upon exposure to HCCMF.

2.20. Long-term antitumour effect in a patient with advanced hepatocellular carcinoma

A 79-year-old man, diagnosed with hepatocellular carcinoma in January 2011, underwent left hepatectomy in February 2011. Histologic review revealed a 10-cm lesion consistent with poorly differentiated hepatocellular carcinoma with negative margins, pT3NxMx. Recurrent disease was identified by radiologic imaging in May 2011 revealing four new lesions within the right lobe of the liver. The patient underwent chemoembolization of the liver lesions with lipiodol and doxorubicin in June 2011. Follow-up magnetic resonance imaging (MRI) obtained in July 2011 showed intrahepatic progression of disease. The patient started sorafenib on August 15, 2011 and compassionate use treatment with the TheraBionic device on September 15, 2011. As shown on Fig. S4 the patient had a complete response by AFP marker and a partial response as assessed by imaging studies, which lasted more than six years.

3. Results

3.1. Whole-body and organ-specific dosimetry

Intrabuccal administration of AM RF EMF has yielded objective tumour shrinkage in the femur [8], adrenal gland [8], liver [10], and lungs [10] of patients suffering from unresectable or metastatic cancer (Fig. 1a, b). This strongly suggests that intrabuccally-administered 27·12 MHz AM RF EMF have systemic anticancer effects distant from the point of administration, i.e., the buccal mucosa. However, the levels of AM RF EMF exposure in humans have not yet been characterized. Therefore, we tested the hypothesis that intrabuccal administration of AM RF EMFs results in absorption throughout the body because contact between the spoon-shaped “antenna” applicator and the anterior part of the patient’s tongue could result in the patient’s body acting as an extension of the antenna [11].

The RF output of the AM RF EMF emitting device is adjusted to 100 mW into a 50 Ω load using a sinusoidal test signal [8,10]. We assessed the SAR level and distribution inside the human body and quantified the variability depending on device positioning and patient posture (Fig. 1c). Homogeneous and inhomogeneous model simulations show similar SAR distribution patterns (Fig. 1d, e). The whole-body (wbSAR) and the peak spatial SAR (psSAR) over any 10 g (psSAR10g) and 1 g (psSAR1g) of major organs according to IEEE standard [22] are listed in Table 1a. As shown in Fig. 1d and e, intrabuccal delivery of 27·12 MHz AM RF EMF results in whole-body absorption from head to toe and the highest peak spatial SAR (psSAR) is at the interface between the tongue and the spoon-shaped applicator. As shown in Table 1b, there is more radiated power when the device is far away from the body. Conversely, the wbSAR is slightly higher when the device touches the body, regardless of position (Table 1c). Experimental validation measurements based on a tank phantom show that the SAR distribution inside the tank is similar to that of the homogeneous human model (Fig. 1e, Supplemental Fig. S1a, S1b). The wbSAR is 1·35 mW/kg with psSAR over 1 g from 146 to 352 mW/kg when the applicator spoon is perfectly matched, which is significantly below the International Commission on Non-Ionizing Radiation Protection (ICNIRP) standard safety limits of 80 mW/kg wbSAR, or psSAR of 2000 mW/kg (Table 2) [23]. Organ-specific SAR ranges from 0·02 to 1 mW/kg (Table 2).

Uncertainty and variation assessments were conducted with the patient sitting with the device placed away from the body (Fig. 1c). The posture variation based on sitting positions as shown in Fig. 1c introduces 0·06 dB deviation. A \pm 10 kg variation in body weight introduces 0·39 dB deviation, the biggest contribution, 2·19 dB comes from the variation of the applicator spoon impedance with posture and device position and its effect on the power delivered to the patient. Therefore, the total variation of 2·21 dB, as shown in Table 1d, mainly depends on

the delivered power. The SAR distributions along the centre line inside the tank phantom are compared to the simulations of the same configurations (Supplemental Fig. S1a) to determine the effective power delivered by the spoon-shaped applicator as a function of the positioning of the device. The effective power per device location is shown in Supplemental Table S1a. Based on the delivered power, and the power delivered when matched, the effective return loss can be calculated and is also shown in Supplemental Table S1a. In the real use scenario, the delivered power is between 11 and 51% of the perfectly matched case. Reflection coefficient measurements of the applicator spoon were performed with a portable vector network analyser, Supplemental Fig. S1c, Supplemental Table S1b; when compared to those calculated based on normalized fields, more than one effect must be present, namely, impedance dependent output power variation as well as mismatch. Consideration not only of the induced field levels, but also the field distributions inside the rectangular phantom, shows that the measurements and simulations are generally in agreement, as shown in Supplemental Fig. S1a for configurations 1 and 3 in Fig. 1e, which are equivalent to the sitting position with the device on the thigh and a short distance away from the body, respectively. The differences are larger in locations with low field strength, e.g., at the far end of the phantom from the applicator spoon, as the induced field strengths are close to or below the measurement system noise floor. This is especially evident in cases where the mismatch is largest and delivered power is low. E-field measurements normalized to the same delivered power, for lines in the middle and along the bottom of the phantom for the different positions of the device, are shown in Supplemental Fig. S1b. Away from the immediate vicinity of the applicator spoon, there is not much difference between the two distributions along the tank, as might be expected; locations close to the surface are more sensitive to the device location.

3.2. In vivo effects of amplitude-modulated radiofrequency electromagnetic fields

Having characterized SAR levels delivered to patients during treatment with the AM RF EMF emitting device, we set out to replicate human exposure conditions in vivo. We used a custom-designed small animal AM RF EMF exposure system [14] and exposed tumour-bearing mice with tumours developing in subcutaneous tissue predominantly surrounded by fat. The exposure system RF output was set for delivery of a SAR level of 67 mW/kg. This SAR was selected so that it is 1) within the range of previously demonstrated in vitro activity (30–400 mW/kg) [9] and 2) within the range of wbSAR1g and psSAR1g in patients receiving treatment with the TheraBionic device (1–352 mW/kg) (Table 2). We used Huh7 and patient-derived tumour cells as subcutaneous cellular xenograft models of HCC [24–26]. Thirty-seven of 40 mice injected with Huh7 cells developed palpable tumours and were exposed to HCC-specific AM RF EMF (HCCMF), randomly chosen AM RF EMF (RCF), or were not exposed to EMF (SHAM) as controls. Both control subsets (RCF and no exposure) were compared to the group exposed to HCC-specific frequencies ($N = 20$). The treatment by time interaction was highly significant ($p < 0\cdot001$) showing that tumour growth curves were different among the three groups. Comparison between the two control subsets showed no statistical difference over the course of six weeks; $p = 0\cdot655$. The two groups were therefore combined as control group. Comparison between the pooled control group ($N = 17$) and the HCCMF ($N = 20$) group shows beginning separation between groups at week four ($p = 0\cdot08$), and significant separation at week five ($p = 0\cdot045$), and week six ($p = 0\cdot019$) (Fig. 2a). We applied the commonly used RECIST 1.1 criteria [27] to assess response to treatment. At week six, the volume of 8 (42·1%) of the 19 tumours exposed to HCCMF had decreased by 30% or more. At the same time point none of the 17 tumours of the control group had evidence of shrinkage (Supplementary Fig. S1d).

Table 1
Organ-specific SAR with the device on the thigh or away from the body.

| (a) | | | | | | |
|--------------------|--------------------------|---------|--------|----------------------|---------|--------|
| Organ-specific SAR | Device on thigh (case 1) | | | Device away (case 3) | | |
| | Mean | PS-10 g | PS-1 g | Mean | PS-10 g | PS-1 g |
| Whole body | 13.5 | 2583 | 6900 | 13.4 | 3399 | 9110 |
| Brain grey matter | 2.2 | 10.1 | 15.7 | 2.5 | 14.2 | 22.1 |
| Brain white matter | 1 | 3 | 4.6 | 1 | 3.5 | 6.3 |
| Midbrain | 3.7 | 3.9 | 5.4 | 3.9 | 4.2 | 5.9 |
| Heart | 7.7 | 13.7 | 15.8 | 4.9 | 8.1 | 9.3 |
| Liver | 8.4 | 16 | 29.2 | 4.2 | 7.5 | 14.7 |
| Lung | 13.9 | 59.7 | 92.1 | 11.2 | 63.7 | 99.6 |

| (b) Simulation power budget for a homogeneous human model, nominal input power 1 W | | | | |
|--|-------|-------|-------|-------|
| Body/device positions | 1 | 2 | 3 | 4 |
| Mean SAR (mW/kg/W) | 13.4 | 13.4 | 13.2 | 10.1 |
| Std. deviation (mW/kg/W) | 44.6 | 57.4 | 50.2 | 61.6 |
| Conductivity loss (W) | 0.978 | 0.977 | 0.967 | 0.723 |
| Radiated power (W) | 0.003 | 0.003 | 0.012 | 0.262 |
| Total power (W) | 0.98 | 0.98 | 0.98 | 0.99 |

| (c) Simulation power budget for rectangular tank phantom, nominal input power 1 W | | | | |
|---|--------|--------|--------|--------|
| | Case 1 | Case 2 | Case 3 | Case 4 |
| Mean SAR (mW/kg/W) | 74.5 | 75.4 | 72.6 | 60.5 |
| Std. deviation (mW/kg/W) | 90.3 | 148.8 | 129.2 | 120.8 |
| Conductivity loss (W) | 0.993 | 0.99 | 0.987 | 0.807 |
| Radiated power (W) | 0.001 | 0.001 | 0.004 | 0.185 |
| Total power (W) | 0.99 | 0.99 | 0.99 | 0.99 |

| (d) Variation assessment during the use of the TheraBionic device | | | | |
|---|----------|-------|------|---------------|
| Contributions | Unc (dB) | Distr | Div | Std. Unc (dB) |
| Posture | 0.11 | R | 1.73 | 0.06 |
| Weight deviation (± 10 kg) | 0.66 | R | 1.73 | 0.39 |
| Applicator spoon matching | 3.3 | R | 1.73 | 2.19 |
| Combined standard variation ($k = 1$) | | | | 2.21 |

To characterize *in vivo* the temporal relationship between exposure to HCCMF and HCC growth, we randomly selected and studied five mice, which had been exposed to RCF 3 h daily for ten weeks, all of which had evidence of tumour growth while exposed to RCF (Suppl. Fig. 7). As shown in Fig. 2b, the growth of Huh7 xenografts stopped within one week of switching from exposure RCF to exposure to HCCMF (week 11) and the tumours shrank by 62% within three weeks of exposure to HCCMF. To assess the carry-over effect of HCCMF, we stopped exposure at the end of week 14. As shown in Fig. 2b, the average volume of Huh7 xenografts increased by 109% within two weeks. To determine whether repeat exposure to HCCMF could again block tumour growth, mice were re-exposed to HCCMF at week 15. As shown in Fig. 2b and Suppl. Fig. 7 tumour growth was, again, effectively blocked within one week of re-exposure. Lastly, to assess *in vivo* the effect of HCCMF on patient-derived xenografts (PDX), we exposed 6 PDX mice to HCCMF. Four PDX mice were observed as controls. As shown in Fig. 2c, tumour growth was significantly inhibited by HCCMF, test for treatment by time interaction ($p = 0.0006$).

Table 2
Organ-specific SAR.

| Organs | Mean SAR (mW/kg) | psSAR 1 g (mW/kg) |
|--------------------|------------------|-------------------|
| Whole body | 0.20–1.00 | 146.00–352.00 |
| Brain grey matter | 0.04–0.20 | 0.20–0.60 |
| Brain white matter | 0.02–0.10 | 0.05–0.15 |
| Midbrain | 0.06–0.20 | 0.06–0.20 |
| Heart muscle | 0.05–0.50 | 0.10–1.00 |
| Liver | 0.05–0.50 | 0.10–1.00 |
| Lung | 0.20–1.00 | 1.00–4.00 |

In summary, we observed significant tumour shrinkage ranging from near complete and partial responses to tumour stabilization in two different mouse models of HCC, which establishes that HCCMF exert sustained control over the growth of HCC tumours *in vivo* at SAR levels corresponding to the levels delivered in patients with advanced HCC. In contrast, there was no shrinkage in any tumours exposed to randomly chosen frequencies or not exposed to any EMF.

3.3. Tumour shrinkage is associated with HCC cell differentiation into quiescent cells with spindle morphology

Having demonstrated that exposure to HCCMF results in shrinkage of Huh7 tumour xenografts, similarly to what has been observed in patients receiving treatment with HCCMF, we examined the histology of shrunken tumours and tumours from the control group. The first difference between tumours treated with HCC-specific AM RF EMF compared with control tumours was the absence of necrosis (Supplementary Fig. S5). Second, we consistently observed accumulation of fibroblast-like cells around and intermeshed with the shrunken HCC xenografts suggesting that fibroblast-like cells had replaced HCC cells (Fig. 3a). To identify the origin of these cells, we used green-fluorescent protein (GFP) tagged Huh7 cells.

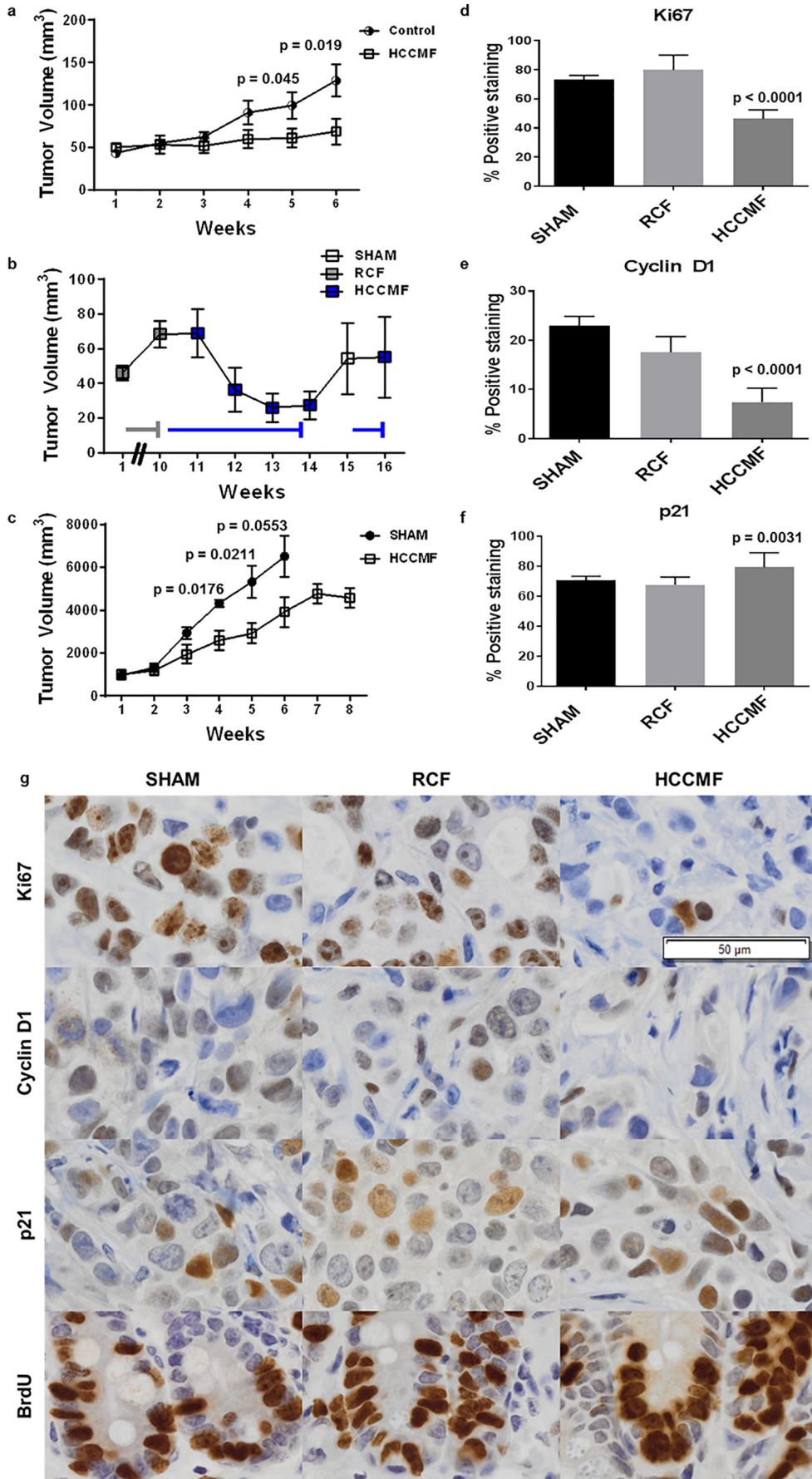
As shown in Fig. 3b, there was strong GFP staining of the fibroblast-like cells surrounding and intermeshed with residual Huh7 cells demonstrating their HCC origin. To further characterize these cells, we performed immunohistochemistry analysis of several fibroblast cell markers. As shown in Fig. 3c-d, marker analysis identified two separate subpopulations of fibroblast-like cells in shrunken tumours compared to control tumours, a peripheral region surrounding a distinct central region. The peripheral cells were positive for E-cadherin, fibronectin, and TWIST, weakly positive for smooth muscle actin (SMA) and faintly positive for SNAIL while the centrally located cells were more intensely positive for fibronectin and SMA but did not stain for E-cadherin, N-cadherin and SNAIL and had decreased staining for TWIST (Fig. 3c). As shown in Supplementary Fig. S6 the tumours exposed to HCCMF show central hyalinization with increased staining intensity of trichrome, fibronectin and SMA in contrast to control tumours exposed to either RCMF or SHAM, which show multiple foci of necrosis without any evidence of hyalinization. These findings suggest that centripetal tumour shrinkage during exposure to HCCMF results in the differentiation of HCC cells into quiescent cells with spindle morphology at the centre with residual carcinoma-like cells at the periphery of the shrunken tumour.

To test the hypothesis that HCCMF only targets the proliferation of HCC cells in mice carrying tumour xenografts, we assessed tumour Ki67 as well as intestinal crypt BrdU staining in mice in which HCCMF had yielded at least 55% tumour shrinkage as well as in control mice. As shown in Fig. 2d-f, Ki67 and cyclin D1 staining was decreased and p21 increased in the tumours of mice exposed to HCCMF compared to control mice. However, there was no difference in intestinal crypt BrdU staining between mice exposed to HCCMF and control mice (Fig. 2g). Similarly, there were no differences in white blood cells, red blood cells and platelets between HCCMF-exposed and control mice at the time of sacrifice (Supplemental Table S2a).

In summary, HCCMF target HCC cell proliferation *in vivo* and tumour shrinkage occurs through HCC cells differentiation into quiescent cells with spindle morphology.

3.4. HCCMF antiproliferative effects require calcium influx through $Ca_v3.2$ T-type voltage gated calcium channels (CACNA1H)

To agnostically assess the impact of HCCMF on HCC, we performed a combined review of the previously published RNA-Seq data [9] and new microRNA array assays. Ingenuity pathway analysis identified the IP3/DAG signalling pathway through differential expression of several genes and microRNAs (Supplemental Fig. S3a). Differential expression



of several key genes and microRNAs modulating this pathway was confirmed in Huh7 cells (Supplemental Fig. S3b). Ca^{2+} modulates several steps of this pathway [28], and we and others [29] have shown that Ca^{2+} flux from brain tissue is enhanced upon exposure to RF EMF but only when modulated at specific frequencies, irrespective of the carrier frequency used (50, 147, and 450 MHz) [30]. We therefore postulated that Ca^{2+} is involved in HCCMF antiproliferative effects on HCC cells. To begin to test this hypothesis, we added BAPTA, a chelator of Ca^{2+} , during each HCCMF exposure. As shown in Fig. 5a, chelation of extracellular Ca^{2+} abrogates HCCMF antiproliferative effects without affecting the proliferation of Huh7 cells exposed to RCF demonstrating that extracellular Ca^{2+} plays a central role in this process.

Next, we sought to determine if extracellular Ca^{2+} enters HCC cells upon exposure to HCCMF. As shown in Supplemental Fig. S3c, there was an increase in intracellular Ca^{2+} following exposure to HCCMF. We validated changes in intracellular Ca^{2+} following exposure to HCCMF with Fluo-4 calcium imaging. As shown in Fig. 4, intracellular Ca^{2+} was significantly increased after exposure of HCC cells (Huh7) to HCCMF for 30 min, 1 h, 3 h, and 6 h. We additionally validated increased intracellular Ca^{2+} in a second cell line (Hep3B) at the three-hour time point (Fig. 4). However, no increase in intracellular Ca^{2+} was observed after exposure to either RCF or breast cancer-specific AM RF EMF (data not shown). Moreover, there were no changes in intracellular Ca^{2+} levels when culturing cells in Ca^{2+} -free medium demonstrating that HCCMF-mediated increase in intracellular Ca^{2+} is due to Ca^{2+} influx from the extracellular to the intracellular compartment, not by mobilization of intracellular Ca^{2+} stores. Lastly, HCCMF exposure did not have an impact on intracellular Ca^{2+} levels in human non-malignant hepatocytes (THLE2; ATCC), human microglia cells (HMC3; ATCC) or Rat myocardium cells (H9c2; ATCC) (data not shown) demonstrating that Ca^{2+} influx is both tumour- and tissue-specific as it only occurs when HCC cells are exposed to HCCMF.

Having demonstrated that extracellular Ca^{2+} influx was necessary for HCCMF inhibition of HCC cell proliferation, we sought to identify how Ca^{2+} enters the cells. Ca^{2+} entry is mainly controlled by voltage-gated Ca^{2+} channels (VGCCs) [31–33]. We used inhibitors of L-type and T-type VGCCs to determine whether these VGCCs are involved in HCCMF Ca^{2+} influx and inhibition of cell proliferation. Amlodipine, which blocks L-type VGCCs, did not alter Ca^{2+} influx (data not shown). In contrast, ethosuximide, which blocks all three T-type VGCCs ($\text{Ca}_v3.1$, 3.2 , 3.3) [34], abrogated HCCMF's Ca^{2+} influx as well as inhibition of Huh7 cell proliferation (Fig. 5b). Having identified T-type VGCCs as the necessary mediators of HCCMF Ca^{2+} influx and inhibition of HCC cell proliferation, we asked which of the three T-type VGCCs isoforms accounted for this effect. While knockdown of $\text{Ca}_v3.1$ (CACNA1G) and $\text{Ca}_v3.3$ (CACNA1I) did not affect HCCMF-mediated inhibition of HCC cell proliferation, knockdown of $\text{Ca}_v3.2$ (CACNA1H) abrogated HCCMF antiproliferative effects in Huh7 and Hep3B cell lines (Fig. 5c).

In summary, HCCMF exert their selective antiproliferative effects on HCC cells by targeting CACNA1H, an event contingent on Ca^{2+} influx into HCC cells, an event restricted to HCC cells.

3.5. HCCMF block HCC cancer stem cells

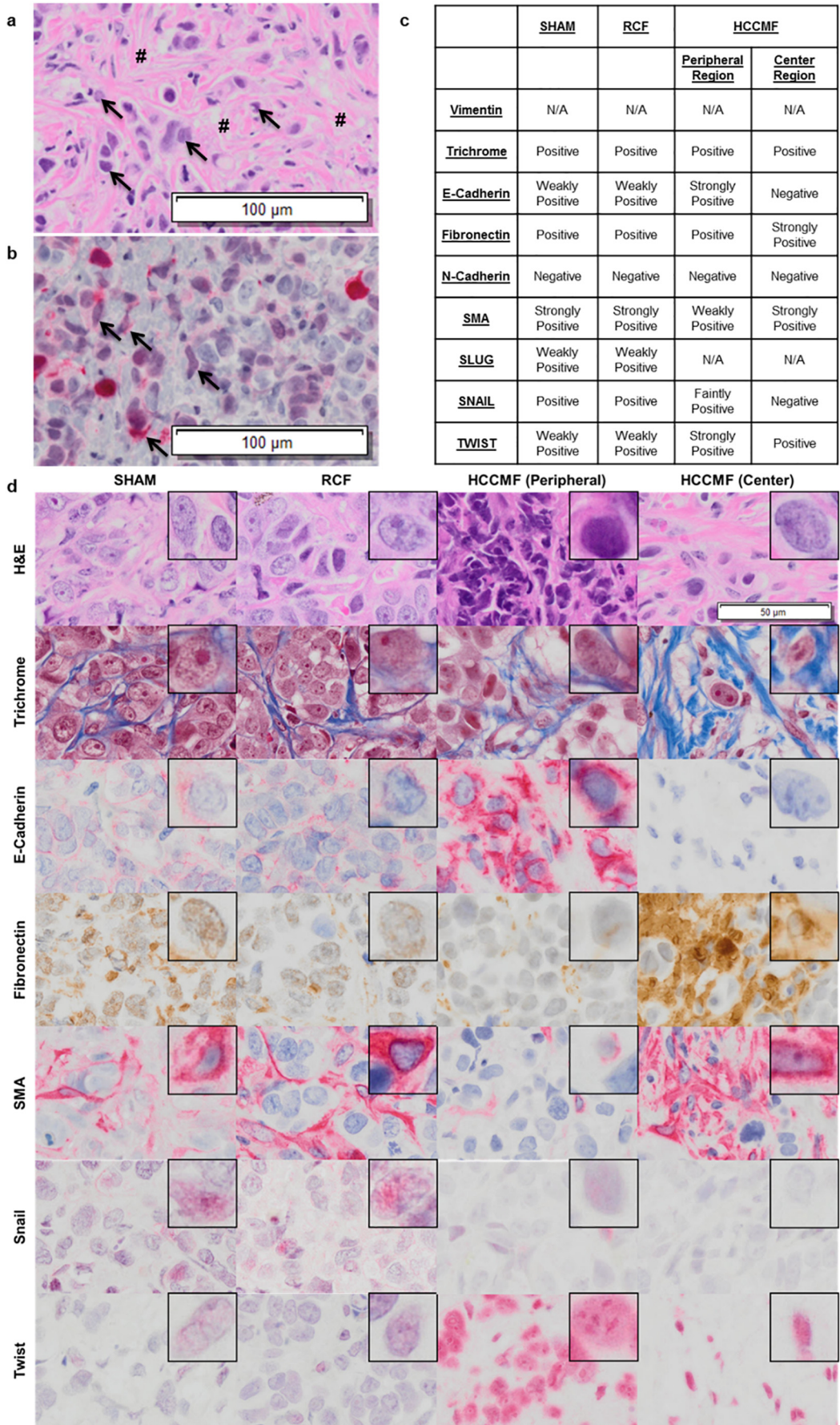
It has been shown that sorafenib and lenvatinib significantly improve the survival of patients with advanced HCC [4,35,36]. However, patients invariably develop resistance to both agents [4,35–37] as exemplified by the fact that all 954 patients enrolled in a recent study comparing sorafenib and lenvatinib had died 42 months after enrollment [4]. There is growing evidence that HCC cancer stem cells (CSCs) are responsible for tumour recurrence and resistance to sorafenib [38–40]. We have previously reported several long-term responses in patients with advanced HCC receiving intrabuccally administered AM RF EMF. Specifically, 6 (14.6%) of the 41 patients had an overall survival in excess of 26 months, one patient was treated continuously for 44.6 months, and one patient was treated continuously for 62 months without any evidence of disease progression prior to expiring of causes unrelated to her malignancy [10,11]. One additional off-study patient with rapidly progressive disease received continuous treatment with HCCMF for 74 months prior to expiring with minimal progression of disease (Supplemental Fig. S4). These unexpectedly long-lasting responses, which have not been observed with the use of either sorafenib or lenvatinib [4], led us to test the hypothesis that HCCMF target CSCs as therapies affecting CSCs are associated with long-term survival [41].

We first assessed the anti-proliferative effects of HCCMF on hepatitis B virus (HBV) positive cell lines as 53% of HCC cases worldwide are attributable to HBV infection [42]. As shown in Fig. 5d, the proliferation of HBV positive HCC cell lines from patients of Asian (HCLM3 and MHCC97L) and African-American (Hep3B) ancestry was effectively blocked by HCCMF. Next, we assessed the impact of HCCMF on HBV negative (Huh7) and HBV positive (Hep3B) CSCs. As shown on Fig. 5e, exposure to HCCMF led to 57% and 38% decreases in Huh7 and Hep3B CSCs ($\text{CD44} + \text{CD133} +$) cells, respectively. Sphere formation was similarly decreased by 26% and 28% in Huh7 and Hep3B cells, respectively. However, in the presence of ethosuximide, there were no changes in CSCs or sphere formation in either Huh7 or Hep3B cells demonstrating that inhibition of CSCs is also mediated by T-type VGCCs (Supplemental Fig. S2a–d). The experiments were repeated with cells in which CACNA1H had been knocked down. As shown in Fig. 5f, knockdown of CACNA1H abrogated HCCMF downregulation of CSCs in Huh7 as well as Hep3B cells.

4. Discussion

Dosimetry analysis shows that 27.12 MHz AM RF EMF administered by means of a spoon-shaped applicator results in systemic EMF absorption, which is more than one hundred fold lower than the SAR

Fig. 2. Antiproliferative effects of HCCMF in vivo. a, Mice were exposed to either HCCMF exposure with a xenograft-specific SAR of 67 mW/kg or are assigned to the control treatment group 3 h per day. Control group is comprised of mice receiving either randomly chosen frequencies (RCF) with a xenograft-specific SAR of 67 mW/kg and those receiving no exposure (SHAM). Tumour volume is measured three times per week and volume is calculated as $(\text{Length} \times (\text{Width})^2) / 2$. After six weeks of exposure, statistical significance between treated and control groups has been achieved; [Week five ($p = 0.045$), Week six ($p = 0.019$) Student's two-tailed t -test] and [Test for treatment by time interaction ($p < 0.001$)]. b, Sequential exposure to randomly chosen and HCCMF. Five mice carrying Huh7 xenografts were exposed to RCF (grey line) 3 h per day for ten weeks during which the average tumour volume increased by 48%. Exposure was switched to HCCMF (blue line) after ten weeks. Exposure to EMF was discontinued for one week after four weeks exposure, then resumed. Mice were sacrificed at the end of week 16. c, Patient-derived HCC xenografts (PDX) exposed to HCCMF or not exposed to EMF. Patient derived xenografts from a 63-year-old male with hepatocellular carcinoma. Mice received either HCCMF exposure (HCCMF; $N = 6$) or received no treatment (SHAM; $N = 4$). Tumour volume measured three times per week and volume is calculated as $(\text{Length} \times \text{Width}^2) / 2$. After eight weeks of exposure, statistical significance had been achieved; [Week four ($p = 0.0176$), Week five ($p = 0.0211$) Student's two-tailed t -test]. At week six, all mice in the Sham group expired and tumour volume was imputed, Week six ($p = 0.0553$) [student's t -test]. [Test for treatment by time interaction ($p = 0.0006$)]. d, Ki-67 staining of SHAM, RCF and HCCMF treated tumours. [Anova: $F = (2, 33) 67.55, p \leq 0.0001$]. [Post-Hoc Tukey Test: Sham vs RCF $p = 0.2067$, SHAM vs HCCMF $p < 0.0001$, RCF vs HCCMF $p < 0.0001$]. e, Cyclin D1 staining of SHAM, RCF and HCCMF treated tumours. [Anova: $F = (2, 33) 23.29, p < 0.0001$]. [Post-Hoc Tukey test: Sham vs RCF $p = 0.1379$, SHAM vs HCCMF $p < 0.0001$, RCF vs HCCMF $p = 0.0005$]. f, p21 staining of SHAM, RCF and HCCMF treated tumours [Anova: $F = (2, 33) 6.907, p = 0.0031$]. [Post-Hoc Tukey test: Sham vs RCF $p = 0.7373$, Sham vs HCCMF $p = 0.0411$, RCF vs HCCMF $p = 0.0049$]. g, IHC of Huh-7 Xenograft tumours and all images at 20X (Lens; scale bar is 50 μm). Tumour and intestinal crypt cell proliferation in mice exposed to HCCMF, RCF, and mice not exposed to EMF. Representative figures and graphs (d–f) represent mean \pm SEM (SHAM: $N = 3$; RCF: $N = 3$; HCCMF: $N = 6$) and three randomly selected fields of view per slide were used to quantify all staining. BRDU staining of SHAM, RCF and HCCMF treated tumours showed positive staining in all crypts; no statistics performed.



generated by cell phones and does not result in heating of any body part. In all conditions studied, the device complies with the two standards for human exposure to RF EMF, the ICNIRP [23] and the IEEE [22]. The results also demonstrate that the human body acts as an antenna resulting in head to toe delivery of AM RF EMF. These findings provide a biophysical rationale for the antitumor effects documented in patients with metastases in the femur, liver, adrenal glands, lungs, and brain (Sharma et al., manuscript co-submitted with this one) [8,10]. Tumour-specific AM RF EMF appear to have a broad therapeutic window as tumour shrinkage was observed in humans [8,10], in human xenografts as presented in this report, and *in vitro* [9] at SARs ranging from 0.02 mW/kg to 400 mW/kg.

The animal experiments faithfully reproduce the antitumor effects observed in patients with advanced HCC [10] by demonstrating the antitumor activity of HCCMF with partial responses and significant inhibition of cell proliferation in Huh7 as well as patient xenografts derived from surgical samples. These experiments show that the small animal exposure system [14] replicates human AM RF EMF exposure conditions [8,10] in mice and illustrate the targeted antitumor effects of HCCMF resulting in measurable tumour shrinkage without affecting non-tumour proliferating cells. Notably, necrosis was absent among tumours exposed HCCMF while it was a common finding among tumours exposed either to RCF or not exposed to EMF, a phenomenon potentially attributable to the lack of oxygen and blood in larger, growing tumours.

The lack of antiproliferative activity of RCF confirms *in vivo* the earlier *in vitro* findings [9] and establishes that radiofrequency electromagnetic fields modulated at randomly chosen frequencies (RCF) do not affect HCC proliferation. We have previously shown that HCCMF *in vitro* antiproliferative effect occurs after a week of daily three one-hour exposures. Similarly, the growth of Huh7 xenografts, which had grown while exposed to randomly chosen frequencies, was stabilized within one week of exposure to HCCMF, which is indicative of *in vivo* anticancer effect occurring within the same time interval. The systemic targeted effect of HCCMF in mice is illustrated by tumour reduction and changes in tumour Ki67, cyclin D1, and p21 while the proliferation of intestinal stem cells within the crypts and complete blood counts are unaffected. These findings are consistent with the absence of changes in complete blood counts (CBC) in patients receiving HCCMF, even after several years of treatment [10].

Our findings establish that tumour reduction mediated by HCCMF results from differentiation of HCC into quiescent cells with spindle morphology with centripetal loss of SNAIL staining. The transformation of HCC into quiescent cells with spindle morphology at the centre of the shrinking tumour contrasts with the well-documented association between the EMT phenotype, increased SNAIL expression, and aggressive HCC [43] and unveils a new treatment-related phenotype.

The data presented in this report show that HCCMF block the growth of HCC cells derived from African-American (Hep3B), Asian (Huh7, HCCLM3, MHC97L), and Caucasian (HepG2) [9] patients with HCC, irrespective of HBV status, indicating that HBV positive and negative HCC cells derived from individuals of different ethnic backgrounds respond to the antiproliferative effects of the same HCCMF providing strong support for the novel notion of tumour-specific frequency profile. With respect to CSCs, our results indicate that HCCMF block HBV positive and negative HCC CSCs. This provides a plausible mechanism for the unusually long therapeutic responses observed in several patients with advanced HCC. These findings, together with the observation of a complete response by the alpha-fetoprotein (AFP) tumour marker in a patient receiving a combination of sorafenib and HCCMF provide a

strong rationale for new clinical studies combining HCCMF with either multi-kinase inhibitors or immune oncology therapies.

Our genomic-based approach led to the identification of the IP3/DAG signalling pathway and Ca^{2+} as putative mediators of the HCCMF antiproliferative and CSC-downregulating effects. We identified and characterized Ca^{2+} influx resulting in increased intracellular Ca^{2+} . We then showed that Ca^{2+} flows through CACNA1H, which is selectively sensitive for HCCMF frequencies and mediates both antiproliferative and CSC-downregulating effects. Given the fact that CACNA1H mediates the antiproliferative effects and downregulate CSCs in breast cancer following exposure to breast cancer-specific AM RF EMF [44] ["EBioMedicine (companion paper, in press in this issue)"], we conclude that CACNA1H is the bioantenna for tumour-specific AM RF EMF antiproliferative and CSC-downregulating effects in epithelial tumours. To our knowledge this is the first report of the identification and characterization of a bioantenna sensing athermal AM RF EMF. CACNA1H mediates tumour-specific AM RF EMF Ca^{2+} influx, a process that is both tumour- and tissue-specific, which indicates that cytosolic Ca^{2+} oscillations is interpreted by intracellular downstream effectors, which activate different cellular processes [45]. Importantly, no Ca^{2+} influx was detected in HCC cells if randomly chosen or breast cancer-specific frequencies were used instead of HCCMF confirming the absence of AM RF EMF antiproliferative effects on non-corresponding tumour cells or normal cells.

The importance of CACNA1H in cancer proliferation has been reported in several recent studies across a variety of cancer types [46], including breast carcinoma, retinoblastoma, neuroblastoma, glioma melanoma, and HCC [46,47]. However, this effect does not appear to depend on changes in CACNA1H expression during HCC development [48].

We have previously reported that variation in pulse amplitude constitutes the primary method for identification of tumour-specific modulation frequencies [8], which have subsequently been shown to target cancer cell proliferation in a tumour and tissue-specific fashion [9]. CACNA1H is expressed in both endothelial cells and vascular smooth muscle cells of small arteries, which in turn directly affect pulse amplitude [49]. Hence, CACNA1H is a plausible link between the vascular system, crucial to the tumour-specific frequency identification process [8] and the anticancer effects observed *in vitro*, *in vivo* and in patients with advanced HCC. CACNA1H is also necessary for the differentiation of HCC into quiescent cells with spindle morphology during tumour regression, a phenotype that can only be observed following long term exposure to HCCMF. Given the central role played by Ca^{2+} , the use of calcium channel blockers should be avoided in patients receiving treatment with tumour-specific-AM RF EMF, as they are likely to block the anticancer effects of the treatment as most calcium channel blockers block both L-type and T-type VGCCs [50]. The AM RF EMF mechanism reported here is different from that of alternating electric fields (TFIELDS), which exert their antitumor effects through activation of Ca_v 1.2 [51], not Ca_v 3.2 channels. However, both treatment approaches result in increased levels of cytosolic Ca^{2+} .

In summary, we have identified increased intracellular Ca^{2+} resulting from Ca^{2+} influx through CACNA1H as the necessary and sufficient mechanism triggering antiproliferative and CSC-downregulating effects of non-ionizing, non-thermal RF EMF, which are amplitude-modulated at HCC-specific frequencies. Identification of CACNA1H as the bioantenna for tumour-specific AM RF EMF may have broad implications for the diagnosis and treatment of various forms of cancer.

Fig. 3. Histological analysis of Huh7 xenograft tumours. Tumours were exposed to either no treatment (SHAM), or randomly chosen frequencies (RCF) or HCC-specific frequencies (HCCMF) 3 h daily at a SAR of 67 mW/kg. The selected control tumours (SHAM & RCF) grew in size while tumours exposed to HCCMF shrank by approximately 70%. a, Fibroblast-like cells intermeshed with tumour cells following HCCMF mediated tumour shrinkage. Histological analysis 10X (Lens; scale bar is 100um) shows residual tumour cells (→) surrounded by layers of fibroblast-like cells (#) and occasional lipocytes. b, Epithelial neoplasm (Huh7-GFP tagged cells) intermeshed with vector red positive cells (→) of spindle morphology demonstrating the same cell of origin for the two morphologically different populations 10X (Lens; scale bar is 100um). c, IHC summary of multiple IHC stains for SHAM, RCF, and HCCMF treated tumours. d, IHC staining images of Huh7 tumours following treatment. Images at 20X (Lens; scale bar is 50 um) with upper right embedded image at 60X (lens).

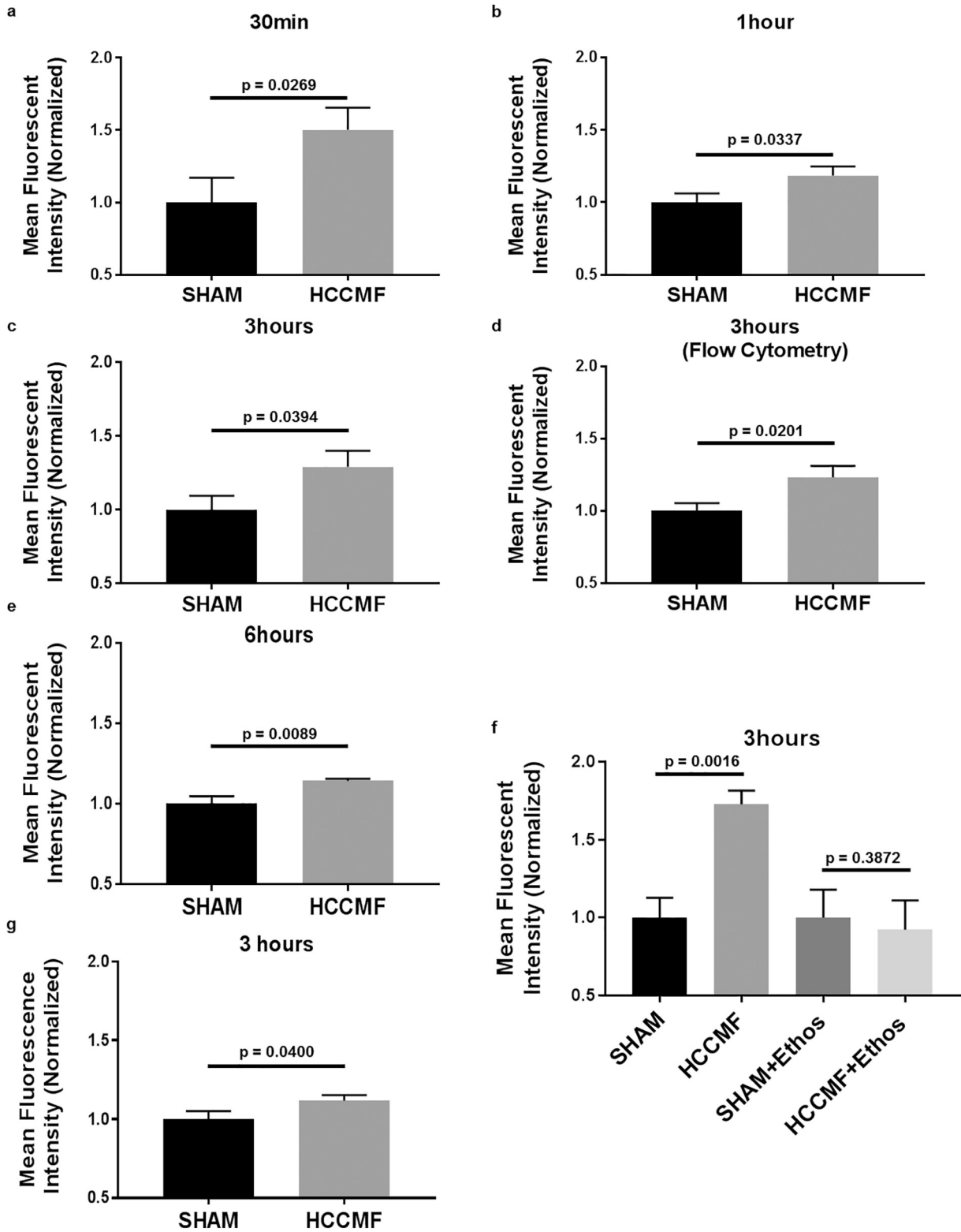


Fig. 4. Intracellular Ca^{2+} measurement in Huh7 and Hep3B cells following exposure to AM RF EMF. a, Huh7: 30 min HCCMF exposure results in 50.2% increase in fluorescence ($p = 0.0296$), $N = 6$ per group. b, Huh7: one-hour HCCMF results in 18.6% increase in fluorescence ($p = 0.0337$), $N = 5$. c, Huh7: three-hour HCCMF results in 29.2% increase in fluorescence ($p = 0.0394$), $N = 5$ per group. d, Huh7: three-hour HCCMF exposure results in 23.2% increase in fluorescence ($p = 0.0201$), $N = 5$ per group. Measured by Flow Cytometry. e, Huh7 six-hour HCCMF exposure of Huh7 cells results in 14.3% increase in fluorescence ($p = 0.0089$), $N = 5$ per group. f, Huh7 three-hour HCCMF results in 72.8% increase in fluorescence ($p = 0.0016$), $N = 6$ per group. There was no increase in intracellular Ca^{2+} in the presence of 0.5 mM Ethosuximide (Ethos) (p -value 0.3872). g, Hep3B three-hour HCCMF exposure of Hep3B cells results in 11.68% increase in fluorescence ($p = 0.0400$), $N = 11$ SHAM & $N = 10$ HCCMF. All fluorescent data was read using a Fluostar fluorescent plate reader (unless otherwise stated i.e. flow cytometry) with 485 excitation/520 emission and calcium staining was accomplished using the Fluo-4 calcium imaging kit (Molecular Probes). All experiments performed at least twice with representative experiments shown. [Student's one-tailed t -test was used to identify statistical significance as Ca^{2+} influx (directionality) was identified and established].

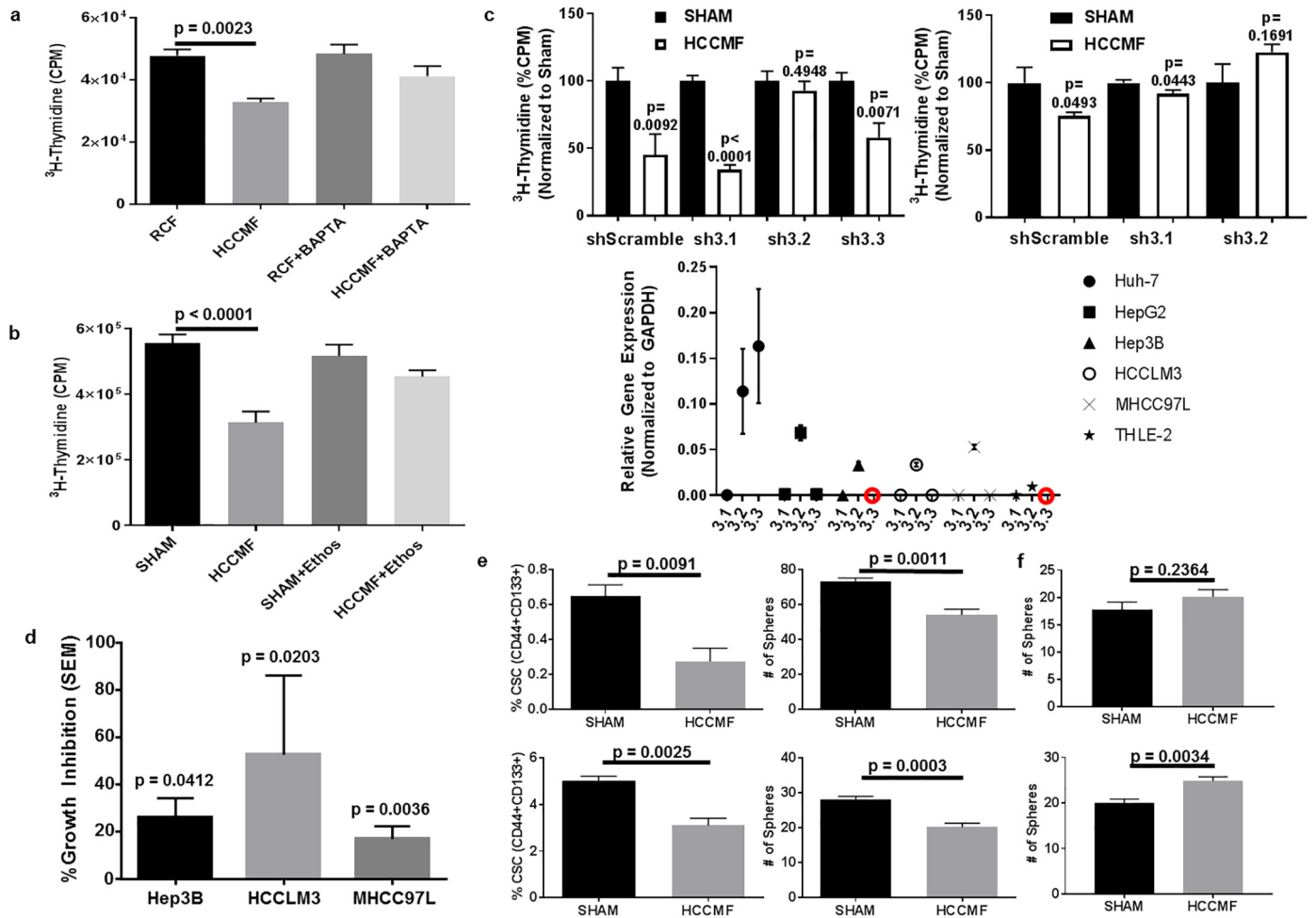


Fig. 5. HCCMF antiproliferative effects on HCC cells and downregulation of CSCs are mediated by Cav 3.2 T-type voltage gated calcium channels (CACNA1H). **a**, Ca^{2+} chelation abrogates AM RF EMF-mediated inhibition of Huh7 cell proliferation. Huh7 cells were exposed to either randomly chosen (RCF) or hepatocellular carcinoma-specific (HCCMF) AM RF EMF 3 h daily for seven days prior to cell proliferation assays with tritiated thymidine incorporation. ANOVA followed by Tukey post hoc-test: [Anova: $F = (3, 20) 8.258, p = 0.0009$] showed that proliferation of cells exposed to HCCMF was significantly lower than cells exposed to RCF [Post-Hoc Tukey Test $p = 0.0023$]. **b**, T-type voltage gated calcium channel blockade with ethosuximide abrogates HCCMF inhibition of Huh7 cell proliferation. Huh7 cells were exposed to HCCMF 3 h daily for seven days prior to cell proliferation assays. Huh7 cells not exposed to AM RF EMF (SHAM) were used as controls. Experiments were performed in the presence or absence of ethosuximide (Ethos). ANOVA followed by Tukey Post Hoc-Test [Anova: $F = (3, 36) = 13.06, p < 0.0001$] indicates that only HCCMF block Huh7 cell proliferation [Post-Hoc Tukey Test: SHAM vs HCCMF $p < 0.0001$]. **c**, Inhibition of cell proliferation by HCCMF in Huh7 and Hep3B cells with selective knockdown of Cav 3-1, Cav 3-2 and Cav 3-3 T-type voltage gated calcium channels. CACNA11 (sh3-3) expression in Hep3B cells was not detectable by qPCR, as noted in Cav isoform relative expression graph, hence knockdown was not attempted. Cell proliferation was assessed after exposure to HCCMF 3 h daily for seven days. Huh7 data (LEFT): shScramble ($N = 5$ for both groups) [Student's two-tailed t-test p value: 0.0092]; sh3-1 ($N = 6$ for both groups) [Student's two-tailed t-test p value: < 0.0001]; sh3-2 ($N = 6$ for both groups) [Student's two-tailed t-test p value: 0.4948]; sh3-3 ($N = 6$ for both groups) [Student's two-tailed t-test p value: 0.0071]. Hep3B data (RIGHT): shScramble ($N = 5$ for SHAM and $N = 6$ for HCCMF) [Student's two-tailed t-test p value: 0.0493]; sh3-1 ($N = 6$ for SHAM and $N = 5$ for HCCMF) [Student's two-tailed t-test p value: 0.0443]; sh3-2 ($N = 6$ for both groups) [Student's two-tailed t-test p value: 0.1691]. (LOWER): Basal expression levels of T-type voltage-gated calcium channels isoforms Cav 3-1, Cav 3-2, and Cav 3-3 in multiple cell lines (RED circles signify with no detectable expression via qRT-PCR). **d**, Antiproliferative effects of HCCMF on HBV positive HCC cells. Cell proliferation was assessed in HCC cells exposed to HCCMF using a [^3H] thymidine incorporation assay as described before. **e**, Effect of HCCMF on HCC cancer stem cells. The cancer stem cell population of Huh7 (upper panel) and Hep3B (lower panel) cells was assessed after one-week exposure to HCCMF. Control cells were not exposed to EMF. The population of cancer stem cells was significantly lower following exposure to HCCMF. (UPPER PAIR) Huh7 %CSC Data: SHAM ($N = 4$) and HCCMF ($N = 4$); [Student's two-tailed t-test p value = 0.0091]. Huh7 Sphere formation: SHAM ($N = 5$) and HCCMF ($N = 5$); [Student's two-tailed t-test p value = 0.0011]. (LOWER PAIR) Hep3B %CSC Data: SHAM ($N = 4$) and HCCMF ($N = 3$); [Student's two-tailed t-test p value = 0.0091]. Hep3B Sphere formation: SHAM ($N = 7$) and HCCMF ($N = 6$); [Student's two-tailed t-test p value = 0.0011]. **f**, Effect of HCCMF on Cav 3-2 knockdown HCC cancer stem cells. The cancer stem cell population of Huh7 Cav3-2 knockdown (upper panel) and Hep3B Cav 3-2 knockdown (lower panel) cells was assessed after one week of exposure to HCCMF. Control cells were not exposed to EMF. The population of cancer stem cells was equal to or greater than the control group following exposure to HCCMF. (UPPER) Huh7 Cav 3-2 knockdown sphere formation: SHAM ($N = 5$) and HCCMF ($N = 5$); [Student's two-tailed t-test p value = 0.2364]. (LOWER) Hep3B Cav 3.2 knockdown sphere formation: SHAM ($N = 6$) and HCCMF ($N = 7$); [Student's two-tailed t-test p value = 0.0034].

Funding sources

Research reported in this publication was supported by the National Cancer Institute's Cancer Centre Support Grant award number P30CA012197 issued to the Wake Forest Baptist Comprehensive Cancer Centre (BP) and by funds from the Charles L. Spurr Professorship Fund (BP). DWG is supported by R01 AA016852 and P50 AA026117. Funders

had no role in study design, data collection, data analysis, interpretation, or writing of this report.

Declarations of interests

Dr. Jimenez has nothing to disclose. Dr. Wang has nothing to disclose. Dr. Xu has nothing to disclose. Dr. Jin has nothing to disclose. Dr.

Lin has nothing to disclose. Dr. Gong has nothing to disclose. Dr. Pennison has nothing to disclose. Dr. Olivier has nothing to disclose. Dr. Yang has nothing to disclose. Dr. Chen has nothing to disclose. Dr. Bonkovsky has nothing to disclose. Dr. Lo has nothing to disclose. Dr. Ghanekar has nothing to disclose. Dr. Watabe has nothing to disclose. Dr. Surratt has nothing to disclose. Dr. Sharma has nothing to disclose. Dr. Zhang has nothing to disclose. Dr. D'Agostino Jr. has nothing to disclose. Dr. Zimmerman has nothing to disclose. Dr. Brezovich has nothing to disclose.

Dr. Chen has nothing to disclose. Dr. Capstick has nothing to disclose. Dr. Liu has nothing to disclose. Dr. DeYoung has nothing to disclose. Dr. Godwin reports grants from NIAAA, during the conduct of the study. Dr. Caudell has nothing to disclose. Dr. Munden has nothing to disclose. Dr. Miller has nothing to disclose. Dr. Blackstock has nothing to disclose. Dr. Absher has nothing to disclose. Dr. Myers has nothing to disclose. Dr. Blackman reports that he has provided a loan to TheraBionic Inc.

Dr. Merle reports other from ONXEO, other from BAYER, other from IPSEN, other from EISAI, other from BMS, other from MERCK, other from ROCHE, other from ASTRA-ZENECA, outside the submitted work.

Dr. Pasche reports grants from NCI P30CA0121978, grants from Charles L. Spurr Professorship Funds, during the conduct of the study; other from TheraBionic Inc., other from TheraBionic GmbH, other from Rafael Holdings, Inc., outside the submitted work; In addition, Dr. Pasche has a patent Europe # 2139557 licensed to TheraBionic Inc., a patent U.S. # 8,977,365 B2 licensed to TheraBionic Inc., a patent Australia # 2008232041 licensed to TheraBionic Inc., a patent Brazil # PI0810084–5 licensed to TheraBionic Inc., a patent Canada # 2,682,322 licensed to TheraBionic Inc., a patent China # ZL 200880009864.4 licensed to TheraBionic Inc., a patent Macau # J/001431 licensed to TheraBionic Inc., a patent Israel # 201099 licensed to TheraBionic Inc., a patent Japan # 5435240 licensed to TheraBionic Inc., a patent South Korea # 10–1,478,582 licensed to TheraBionic Inc., a patent Mexico # 318857 licensed to TheraBionic Inc., a patent Russia # 2594824 licensed to TheraBionic Inc., a patent Saudi Arabia # 3075 licensed to TheraBionic Inc., a patent Singapore # 155671 licensed to TheraBionic Inc., a patent South Africa # 2009/06700 licensed to TheraBionic Inc., and a patent United Arab Emirates # P849/09 licensed to TheraBionic Inc.

Dr. Barbault reports other from TheraBionic Inc., other from TheraBionic GmbH, outside the submitted work; In addition, Dr. Barbault has a patent Europe # 2139557 licensed to TheraBionic Inc., a patent U.S. # 8,977,365 B2 licensed to TheraBionic Inc., a patent Australia # 2008232041 licensed to TheraBionic Inc., a patent Brazil # PI0810084–5 licensed to TheraBionic Inc., a patent Canada # 2,682,322 licensed to TheraBionic Inc., a patent China # ZL 200880009864.4 licensed to TheraBionic Inc., a patent Macau # J/001431 licensed to TheraBionic Inc., a patent Israel # 201099 licensed to TheraBionic Inc., a patent Japan # 5435240 licensed to TheraBionic Inc., a patent South Korea # 10–1,478,582 licensed to TheraBionic Inc., a patent Mexico # 318857 licensed to TheraBionic Inc., a patent Russia # 2594824 licensed to TheraBionic Inc., a patent Saudi Arabia # 3075 licensed to TheraBionic Inc., a patent Singapore # 155671 licensed to TheraBionic Inc., a patent South Africa # 2009/06700 licensed to TheraBionic Inc., and a patent United Arab Emirates # P849/09 licensed to TheraBionic Inc.

Author contributions

Jimenez, H., Wang, M., Zimmerman, J.W., Sharma, S., Xu, Z., Pennison, M., and Surratt, T. contributed directly to data generation and performance of in vitro and in vivo experiments.

Brezovich, I., designed initial cell culture model of EMF exposure device and provided physics related tutoring and initial EMF SAR calculations.

Lin, H.K., Blackstock, A.W., Bonkovsky, H.L. reviewed the manuscript and provided critical comments.

Capstick, M. and Gong, Y. designed and performed dosimetry models, data analysis and write up of final results.

Ghanekar, A. and Chen, K. provided the implanted PDX tumour mouse model.

Watabe, K., Lo, H.W., and Godwin, D.W., provided specialized training in CSC-related cell culture, mouse handling, and Ca²⁺ related tools and signalling to Jimenez, H.

Merle, P., and Munden, R. provided clinical HCC patient information and data review.

Absher, D., Myers, R.M., Miller, L.D., Olivier, M., Jin, G., Liu, L., and Zhang, W. were involved in microRNA and RNA-Seq data generation, analysis and interpretation.

DeYoung, B. and Caudell, D., Yang, G.Y. performed IHC staining, interpretation and overall pathology review.

Jimenez, H. and D'Agostino Jr., R.B. performed all statistics.

Jimenez, H., Blackman, C., Barbault, A., and Pasche, B. designed all experiments, reviewed all data, and were responsible for write up.

All authors have read and agreed to this final version of the manuscript.

Acknowledgements

The authors wish to acknowledge the support of the Wake Forest Baptist Comprehensive Cancer Centre Cancer Genomics, Proteomics, Flow Cytometry, Cellular Imaging, Biostatistics, and Bioinformatics Shared Resource, supported by the National Cancer Institute's Cancer Centre Support Grant award number P30CA012197 and Wake Forest Comparative Pathology Laboratory. The content is solely the responsibility of the authors and does not necessarily represent the official views of the National Cancer Institute. Funders had no role in study design, data collection, data analysis, interpretation, or writing of this report.

Appendix A. Supplementary data

Supplementary data to this article can be found online at <https://doi.org/10.1016/j.ebiom.2019.05.034>.

References

- [1] Siegel RL, Miller KD, Jemal A. Cancer statistics, 2018. *CA Cancer J Clin* 2018;68:7–30. <https://doi.org/10.3322/caac.21442>.
- [2] Islami F, et al. Disparities in liver cancer occurrence in the United States by race/ethnicity and state. *CA. Cancer J Clin* 2017;67:273–89. <https://doi.org/10.3322/caac.21402>.
- [3] Global Burden of Disease Cancer, C. Global, regional, and national cancer incidence, mortality, years of life lost, years lived with disability, and disability-adjusted life-years for 32 cancer groups, 1990 to 2015: a systematic analysis for the global burden of disease study. *JAMA Oncol* 2017;3:524–48. <https://doi.org/10.1001/jamaoncol.2016.5688>.
- [4] Kudo M, et al. Lenvatinib versus sorafenib in first-line treatment of patients with unresectable hepatocellular carcinoma: a randomised phase 3 non-inferiority trial. *Lancet* 2018. [https://doi.org/10.1016/S0140-6736\(18\)30207-1](https://doi.org/10.1016/S0140-6736(18)30207-1).
- [5] Abou-Alfa GK, et al. Cabozantinib in patients with advanced and progressing hepatocellular carcinoma. *N Engl J Med* 2018;379:54–63. <https://doi.org/10.1056/NEJMoa1717002>.
- [6] Zhu AX, et al. Ramucirumab after sorafenib in patients with advanced hepatocellular carcinoma and increased α -fetoprotein concentrations (REACH-2): a randomised, double-blind, placebo-controlled, phase 3 trial. *Lancet Oncol* 2019. [https://doi.org/10.1016/S1470-2045\(18\)30937-9](https://doi.org/10.1016/S1470-2045(18)30937-9).
- [7] Jimenez H, et al. Use of non-ionizing electromagnetic fields for the treatment of cancer. *Front Biosci (Landmark edition)* 2018;23:284–97.
- [8] Barbault A, et al. Amplitude-modulated electromagnetic fields for the treatment of cancer: discovery of tumor-specific frequencies and assessment of a novel therapeutic approach. *J Exp Clin Cancer Res* 2009;28:51. <https://doi.org/10.1186/1756-9966-28-51>.
- [9] Zimmerman JW, et al. Cancer cell proliferation is inhibited by specific modulation frequencies. *Br J Cancer* 2012;106:307–13. [10.1038/bjc.2011.10177](https://doi.org/10.1038/bjc.2011.10177).
- [10] Costa FP, et al. Treatment of advanced hepatocellular carcinoma with very low levels of amplitude-modulated electromagnetic fields. *Br J Cancer* 2011;105:640–8.
- [11] Zimmerman JW, et al. Targeted treatment of cancer with radiofrequency electromagnetic fields amplitude-modulated at tumor-specific frequencies. *Chin J Cancer* 2013;32:573–81. [10.5732/2Fjc.013.10177](https://doi.org/10.5732/2Fjc.013.10177).
- [12] Goldberg P. TheraBionic P1 device receives European regulatory approval. *Cancer Lett* 2018;44:19.
- [13] Kirson ED, et al. Disruption of cancer cell replication by alternating electric fields. *Cancer Res* 2004;64:3288–95.

- [14] Capstick M, Gong Y, Pasche B, Kuster N. An HF exposure system for mice with improved efficiency. *Bioelectromagnetics* 2016;37:223–33. <https://doi.org/10.1002/bem.21969>.
- [15] Gosselin MC, et al. Development of a new generation of high-resolution anatomical models for medical device evaluation: the virtual population 3.0. *Phys Med Biol* 2014;59:5287–303. <https://doi.org/10.1088/0031-9155/59/18/5287>.
- [16] Chen K, Ahmed S, Adeyi O, Dick JE, Ghanekar A. Human solid tumor xenografts in immunodeficient mice are vulnerable to lymphomagenesis associated with Epstein-Barr virus. *PLoS One* 2012;7:e39294. <https://doi.org/10.1371/journal.pone.0039294>.
- [17] Dobin A, et al. STAR: ultrafast universal RNA-seq aligner. *Bioinformatics* 2013;29:15–21. <https://doi.org/10.1093/bioinformatics/bts635>.
- [18] DeLuca DS, et al. RNA-SeQC: RNA-seq metrics for quality control and process optimization. *Bioinformatics* 2012;28:1530–2. <https://doi.org/10.1093/bioinformatics/bts196>.
- [19] Love MI, Huber W, Anders S. Moderated estimation of fold change and dispersion for RNA-seq data with DESeq2. *Genome Biol* 2014;15:550. <https://doi.org/10.1186/s13059-014-0550-8>.
- [20] Risso D, Schwartz K, Sherlock G, Dudoit S. GC-content normalization for RNA-Seq data. *BMC Bioinforma* 2011;12:480. <https://doi.org/10.1186/1471-2105-12-480>.
- [21] Risso D, Ngai J, Speed TP, Dudoit S. Normalization of RNA-seq data using factor analysis of control genes or samples. *Nat Biotechnol* 2014;32:896–902. <https://doi.org/10.1038/nbt.2931>.
- [22] IEEE. IEEE standards for safety levels with respect to human exposure to radio frequency electromagnetic fields, 3 kHz to 300 GHz, IEEE C95.1–2005. New York: Institute of Electrical and Electronics Engineers; 2006.
- [23] ICNIRP. Guidelines for limiting exposure to time-varying electric, magnetic and electromagnetic fields (up to 300 GHz). *Health Phys* 1998;74:494–522.
- [24] Schnater JM, et al. Subcutaneous and intrahepatic growth of human hepatoblastoma in immunodeficient mice. *J Hepatol* 2006;45:377–86. <https://doi.org/10.1016/j.jhep.2006.03.018>.
- [25] Sharma D, et al. Adiponectin antagonizes the oncogenic actions of leptin in hepatocellular carcinogenesis. *Hepatology* 2010;52:1713–22. <https://doi.org/10.1002/hep.23892>.
- [26] Ahmed SU, et al. Generation of subcutaneous and intrahepatic human hepatocellular carcinoma xenografts in immunodeficient mice. *J Vis Exp* 2013:e50544. <https://doi.org/10.3791/50544>.
- [27] Eisenhauer EA, et al. New response evaluation criteria in solid tumours: revised RECIST guideline (version 1.1). *Eur J Cancer* 2009;45:228–47.
- [28] Albarran L, Lopez JJ, Salido GM, Rosado JA. In: Rosado Juan A, editor. Calcium entry pathways in non-excitable cells. Springer International Publishing; 2016. p. 3–24.
- [29] Blackman CF, et al. Induction of calcium-ion efflux from brain tissue by radiofrequency radiation. *Bioelectromagnetics* 1980;1:277–83.
- [30] Bawin SM, Kaczmarek LK, Adey WR. Effects of modulated VHF fields on the central nervous system. *Ann NY Acad Sci* 1975;247:74–81.
- [31] Catterall WA. Voltage-gated calcium channels. *Cold Spring Harb Perspect Biol* 2011;3. <https://doi.org/10.1101/cshperspect.a003947>.
- [32] Prevarskaya N, Skryma R, Shuba Y. Ion channels and the hallmarks of cancer. *Trends Mol Med* 2010;16:107–21. <https://doi.org/10.1016/j.molmed.2010.01.005>.
- [33] Prevarskaya N, Skryma R, Shuba Y. Calcium in tumour metastasis: new roles for known actors. *Nat Rev Cancer* 2011;11:609–18.
- [34] Gomora JC, Daud AN, Weiergräber M, Perez-Reyes E. Block of cloned human T-type calcium channels by succinimide antiepileptic drugs. *Mol Pharmacol* 2001;60:1121–32. <https://doi.org/10.1124/mol.60.5.1121>.
- [35] Llovet JM, et al. Sorafenib in advanced hepatocellular carcinoma. *N Engl J Med* 2008;359:378–90.
- [36] Cheng AL, et al. Efficacy and safety of sorafenib in patients in the Asia-Pacific region with advanced hepatocellular carcinoma: a phase III randomised, double-blind, placebo-controlled trial. *Lancet Oncol* 2009;10:25–34.
- [37] Abou-Alfa GK, et al. Phase II study of sorafenib in patients with advanced hepatocellular carcinoma. *J Clin Oncol* 2006;24:4293–300.
- [38] Wang A, Qu L, Wang L. At the crossroads of cancer stem cells and targeted therapy resistance. *Cancer Lett* 2017;385:87–96. <https://doi.org/10.1016/j.canlet.2016.10.039>.
- [39] Tovar V, et al. Tumour initiating cells and IGF/FGF signalling contribute to sorafenib resistance in hepatocellular carcinoma. *Gut* 2017;66:530–40. <https://doi.org/10.1136/gutjnl-2015-309501>.
- [40] Xu Y, et al. MicroRNA-122 confers sorafenib resistance to hepatocellular carcinoma cells by targeting IGF-1R to regulate RAS/RAF/ERK signaling pathways. *Cancer Lett* 2016;371:171–81. <https://doi.org/10.1016/j.canlet.2015.11.034>.
- [41] Jones RJ, Matsui W. Cancer stem cells: from bench to bedside. *Biol Blood Marrow Transplant: J Am Soc Blood Marrow Transplant* 2007;13:47–52. <https://doi.org/10.1016/j.bbmt.2006.10.010>.
- [42] Perz JF, Armstrong GL, Farrington LA, Hutin YJ, Bell BP. The contributions of hepatitis B virus and hepatitis C virus infections to cirrhosis and primary liver cancer worldwide. *J Hepatol* 2006;45:529–38. <https://doi.org/10.1016/j.jhep.2006.05.013>.
- [43] Critelli R, et al. Microenvironment inflammatory infiltrate drives growth speed and outcome of hepatocellular carcinoma: a prospective clinical study. *Cell Death Dis* 2017;8:e3017. <https://doi.org/10.1038/cddis.2017.395>.
- [44] Sharma S, et al. Ca²⁺ and CACNA1H mediate targeted suppression of breast cancer brain metastasis by AM RF EMF. *EBioMedicine* 2019;44:194–208.
- [45] Smedler E, Uhlen P. Frequency decoding of calcium oscillations. *Biochim Biophys Acta* 2014;1840:964–9. <https://doi.org/10.1016/j.bbagen.2013.11.015>.
- [46] Dziegielewska B, Gray LS, Dziegielewski J. T-type calcium channels blockers as new tools in cancer therapies. *Pflugers Arch - Eur J Physiol* 2014;466:801–10. <https://doi.org/10.1007/s00424-014-1444-z>.
- [47] Li Y, et al. A role of functional T-type Ca²⁺ channel in hepatocellular carcinoma cell proliferation. *Oncol Rep* 2009;22:1229–35.
- [48] Zúñiga-García V, et al. Differential expression of ion channels and transporters during hepatocellular carcinoma development. *Dig Dis Sci* 2015;60:2373–83. <https://doi.org/10.1007/s10620-015-3633-9>.
- [49] Mikkelsen MF, Bjorling K, Jensen IJ. Age-dependent impact of Ca_v 3.2 T-type calcium channel deletion on myogenic tone and flow-mediated vasodilatation in small arteries. *J Physiol* 2016;594:5881–98. <https://doi.org/10.1113/jp271470>.
- [50] Kopecky BJ, Liang R, Bao J. T-type calcium channel blockers as neuroprotective agents. *Pflugers Arch* 2014;466:757–65. <https://doi.org/10.1007/s00424-014-1454-x>.
- [51] Neuhaus E, et al. Alternating electric fields (TFields) activate Cav1.2 channels in human glioblastoma cells. *Cancers* 2019;11:110.